ADVANCED FUNCTIONAL MATERIALS
www.afm-journal.de

Reduced Graphene Oxides Modified Bi_2Te_3 Nanosheets for Rapid Photo-Thermoelectric Catalytic Therapy of Bacteria-Infected Wounds

*Siyu Wang, Yuqian Qiao, Xiangmei Liu, Shengli Zhu, Yufeng Zheng, Hui Jiang, Yu Zhang, Jie Shen, Zhaoyang Li, Yanqin Liang, Zhenduo Cui, Paul K. Chu, and Shuilin Wu**

Temperature variation-induced thermoelectric catalytic efficiency of thermoelectric material is simultaneously restricted by its electrical conductivity, Seebeck coefficient, and thermal conductivity. Herein, Bi_2Te_3 nanosheets are in situ grown on reduced graphene oxides (rGO) to generate an efficient photo-thermoelectric catalyst (rGO-Bi_2Te_3). This system exhibits phonon scattering effect and extra carrier transport channels induced by the formed heterointerface between rGO and Bi_2Te_3, which improves the power factor value and reduces thermal conductivity, thus enhancing the thermoelectric performance of 2.13 times than single Bi_2Te_3. The photo-thermoelectric catalysis of rGO-Bi_2Te_3 significantly improves the reactive oxygen species yields, resulting from the effective electron–hole separation caused by the unique thermoelectric field and heterointerfaces of rGO-Bi_2Te_3. Correspondingly, the electrospinning membranes containing rGO-Bi_2Te_3 nanosheets exhibit high antibacterial efficiency in vivo (99.35 ± 0.29%), accelerated tissue repair ability, and excellent biosafety. This study provides an insight into heterointerface design in photo-thermoelectric catalysis.

1. Introduction

Antimicrobial resistance issue has great threat and burden to public health. Therefore, various non-antibiotic strategies are rapidly developed to eradicate drug-resistant bacteria, including materioherbology,[1] photocatalytic disinfection,[2] and photothermal therapy.[3] Recently, photoresponsive materials have emerged as a promising substitute of antibiotics for treating bacterial infections because of increasing multi-drug resistant bacteria including the common methicillin-resistant *Staphylococcus aureus* (MRSA) induced by the abuse of anitbiotics. Besides its versatile, ecofriendly, and energy-efficient characteristics, this kind phototherapeutic antibacterial strategy can kill bacteria by generating heat or reactive oxygen species (ROS) under light irradiation.[2] However, the rapid photogenerated electron-hole recombination results in poor catalytic performance while the local hyperthermia causes great damage to healthy tissues.[3] Currently, the improved strategies (such as surface defect engineering or heterostructure construction, etc.) generally can only enhance the charge separation on the catalyst surface, but cannot effectively suppress the carrier recombination in the catalyst bulk. The electric field is the driving force for the directional migration of charges,[4] so constructing internal electric fields is one of the most promising approaches to achieve electrons-holes

S. Wang, S. Zhu, H. Jiang, Z. Li, Y. Liang, Z. Cui, S. Wu
School of Materials Science & Engineering
the Key Laboratory of Advanced Ceramics and Machining Technology by the Ministry of Education of China
Tianjin University
Tianjin 300072, China
E-mail: slwu@pku.edu.cn

Y. Qiao, Y. Zheng, S. Wu
School of Materials Science & Engineering
Peking University
Beijing 100871, China

X. Liu
School of Health Science and Biomedical Engineering
Hebei University of Technology
Xiping Avenue 5340, Beichen District, Tianjin 300401, China

The ORCID identification number(s) for the author(s) of this article can be found under https://doi.org/10.1002/adfm.202210098.

Y. Zhang
Department of Orthopedics
Guangdong Provincial People's Hospital
Guangdong Academy of Medical Sciences
Guangzhou 510080, China

J. Shen
Shenzhen Key Laboratory of Spine Surgery
Department of Spine Surgery
Peking University Shenzhen Hospital
Shenzhen 518035, China

P. K. Chu
Department of Physics
Department of Materials Science and Engineering
and Department of Biomedical Engineering
City University of Hong Kong
Kowloon, Hong Kong 999077, China

DOI: 10.1002/adfm.202210098

spatial separation, thus improving catalytic performance of photocatalysts.

Thermoelectric technology can directly convert thermal energy into electrical energy, because the temperature difference can induce electron-hole separation in thermoelectric material.[5] The hot end enriched positive charges and the cold end enriched negative charges produce an internal electric field inside the thermoelectric material. Moreover, many photocatalytic processes are accompanied by photothermal phenomena.[6] Given the above background, we hypothesize that converting photothermic to electricity to drive the carrier separation and transport in the semiconductor catalyst is an ideal way to improve catalytic efficiency. Notably, photothermy-driven thermoelectric catalysis can be expected to efficiently generate local heat and ROS through constructing internal thermal electric field and intensifying carrier separation in the synergistic process of photocatalysis, photothermal, and thermoelectricity.

To realize efficient photo-thermoelectric catalysis, the highest possible thermoelectric conversion efficiency or a large thermoelectric figure of merit (ZT) is required.

$$ZT = \left(\frac{S^2\sigma}{\kappa}\right)T \tag{1}$$

In equation (1), S, σ, κ, and T represent the Seebeck coefficient, electrical conductivity, thermal conductivity, and absolute temperature, respectively.[7] Most of these thermoelectric parameters have complex interrelationships due to their mutual dependence on the dynamic carrier concentration n.[8] Therefore, the manipulation and balance of these parameters to optimize the overall thermoelectric performance is essential.

There are various approaches to boost ZT values, such as engineering band structures, trace doping, decoupling thermoelectric parameters, and developing new materials.[9] The common feature of these strategies for optimizing thermoelectric performance includes the improvement of the electrical transport performance and reduction the thermal transport performance. The electrical and thermal conductivity of crystal is closely related to its internal phonons and charge carriers. The lattice atoms in the crystal keep doing micro-vibration motion near their equilibrium position at a certain temperature. Phonons are the energy quantization of lattice vibrations.[10] Therefore, the interaction between lattice and carriers can be regarded as the phonon scattering to carriers. Utilizing this phonon scattering effect inside crystals to regulate the carrier properties may be a universal strategy for optimizing thermoelectric performance.

Bismuth telluride (Bi_2Te_3) is one of the most common and excellent thermoelectric materials near room temperature.[11] Moreover, Bi_2Te_3 possesses excellent photothermal property due to its narrow bandgap.[12] However, the limited thermoelectric performance of Bi_2Te_3 is ascribed to relatively low carrier mobility and high thermal conductivity. To further improve the thermoelectric efficiency of Bi_2Te_3, the additional material with high electrical conductivity and photothermal conversion efficiency (such as reduced graphene oxides (rGO)) is appropriate for constructing the Bi_2Te_3-based heterojunction, which may be expected to achieve the dual function of enhanced phonon scattering effects in heterointerface and extra carrier transport channels. Electrospinning is an emerging technology with simple, low cost and controllable process. Flexible electrospun nanofibers can be widely used in wound dressing, antibacterial protective clothing, filtration, *etc*. Polyurethane (PU) fibers with high elastic recovery, high elongation, and good biocompatibility, are a suitable choice as electrospinning substrates.

Based on the above-mentioned, we propose a hypothesis if a Bi_2Te_3-based composite can be constructed, in which the photothermal effect can trigger the thermoelectric properties and subsequently promote the photocatalytic efficiency, i.e., enhancing the photo-thermoelectric catalytic performance of the composite. According to this hypothesis, in this work, Bi_2Te_3 nanosheets were in situ grown on rGO to generate an efficient photo-thermoelectric catalyst (rGO-Bi_2Te_3). As schematically illustrated in **Scheme 1**, the heterointerface-induced phonon scattering effect and extra carrier transport channels provided by rGO led to improved thermoelectric performance (2.13 times). In photothermy-driven thermoelectric catalysis, the rGO-Bi_2Te_3 nanosheets could accelerate photogenerated charge separation and transfer, further facilitating effective ROS production owing to internal thermal electric field and conductive effect of rGO. The rGO and Bi_2Te_3 in rGO-Bi_2Te_3 nanosheets served as electron receptor and electron donor, respectively, where photogenerated electrons would transfer from Bi_2Te_3 to rGO across their heterointerfaces. Additionally, rGO-Bi_2Te_3 nanosheets were integrated into polyurethane fibers by electrospinning process to form spinning membranes. The functional spinning membrane was used in a MRSA-infected wound healing model, showing excellent disinfection performance, accelerated tissue repair, and reliable biosafety.

2. Results and Discussion

2.1. Characterization of Bi_2Te_3 and rGO-Bi_2Te_3

As schematically illustrated in **Figure 1**a, Bi_2Te_3 nanosheets were obtained by a facile solvothermal method that allow the in situ growth of Bi_2Te_3 on graphene oxide (GO) nanosheets by reduction reaction. The scanning electron microscope (SEM) images of Bi_2Te_3 and rGO-Bi_2Te_3 nanosheets in Figure S1a,b (Supporting Information) exhibited uniform hexagonal nanosheets, which stacked together. The transmission electron microscopy (TEM) image (Figure 1b) more clearly displayed the regular hexagonal of synthesized Bi_2Te_3 nanosheets with the size of ≈600 nm. The uniform elemental mapping distribution of Bi and Te (Figure 1b_1 and 1b_2) by energy dispersive spectrometer (EDS) analysis confirmed the existence of Bi and Te in the synthesized material. The corresponding high-resolution TEM (HRTEM) image in Figure 1b_3 demonstrated the lattice fringe of 0.32 nm, which was indexed as the (015) crystal plane of Bi_2Te_3 crystal.[13] Correspondingly, the TEM image of rGO-Bi_2Te_3 in Figure 1c showed that the rGO nanosheets were successfully composited on Bi_2Te_3 nanosheets. Figure S2a (Supporting Information) presented the irregular flakes of rGO. In addition, the HRTEM image of rGO-Bi_2Te_3 (Figure 1d) also exhibited the typical lattice fringes with 0.32 nm, corresponding to the (015) plane of the Bi_2Te_3 nanosheets.[14] Besides, the HRTEM image of rGO in Figure S2b (Supporting Information)

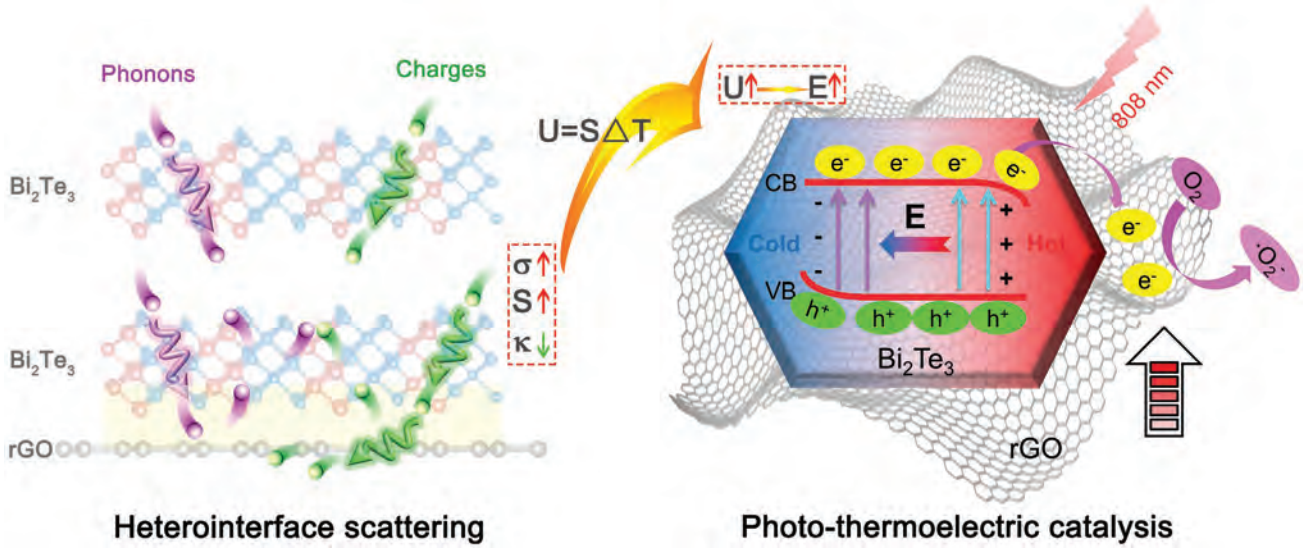

Scheme 1. Schematic illustration of heterointerface scattering and photo-thermoelectric catalysis mechanism. The heterointerface phonon scattering and extra carrier transport channels increased electrical conductivity (σ) and Seebeck coefficient (S) of rGO-Bi_2Te_3, reduced thermal conductivity (κ), and improved overall thermoelectric performance. The enhanced thermoelectric potential and heterointerface carrier separation and transmission effect achieved better photo-thermoelectric catalysis performance.

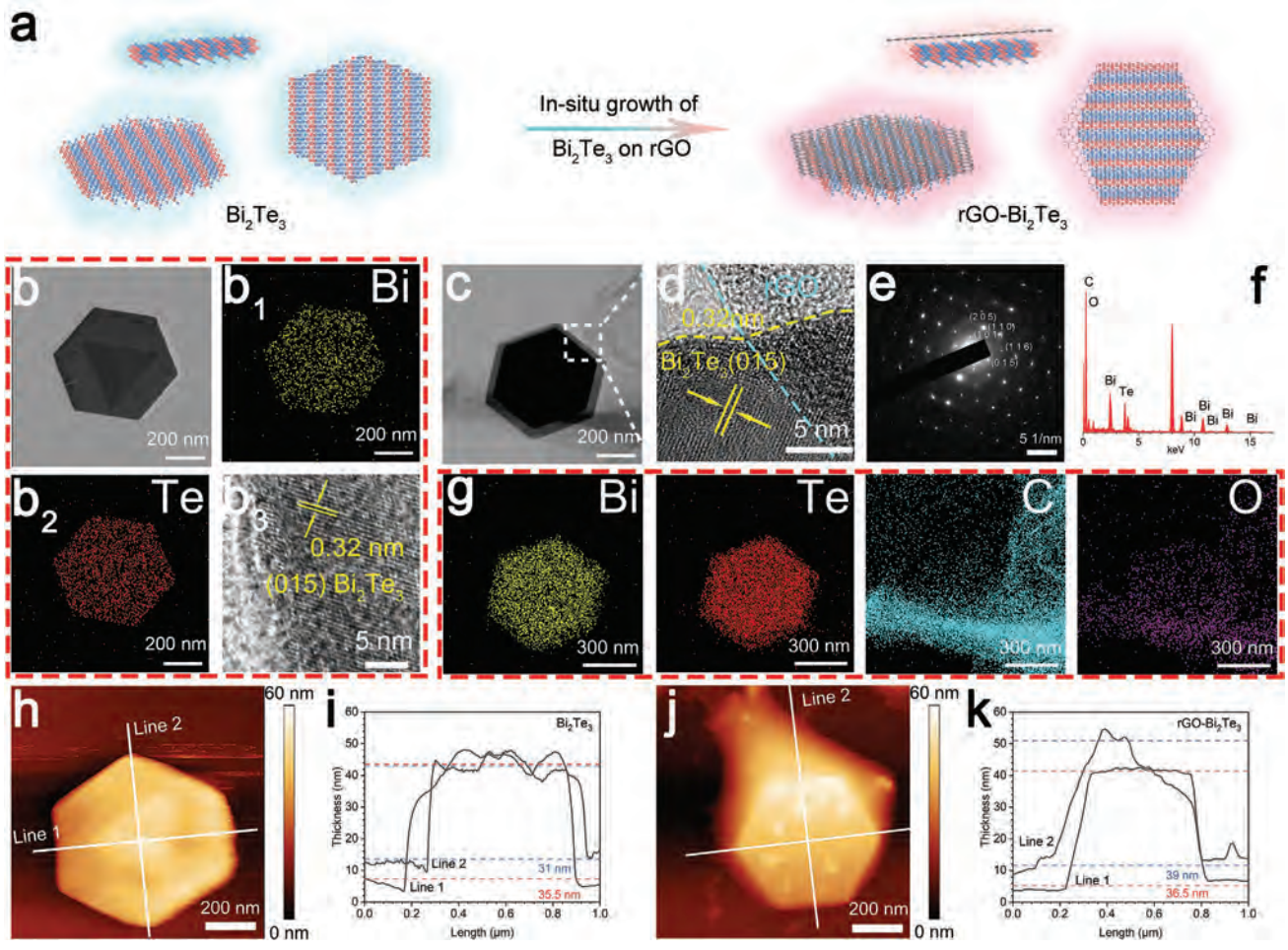

Figure 1. Characterization of prepared materials. a) Schematic illustration of synthesis process of rGO-Bi_2Te_3. b) TEM image, b_1) b_2) EDS elemental mappings, b_3) HRTEM of Bi_2Te_3. c) TEM image, d) HRTEM, e) SAED pattern, f) EDS result, g) EDS elemental mappings of rGO-Bi_2Te_3. The thickness profile of h) and i) a single Bi_2Te_3 nanosheets and j) and k) rGO-Bi_2Te_3 nanosheets analyzed by AFM.

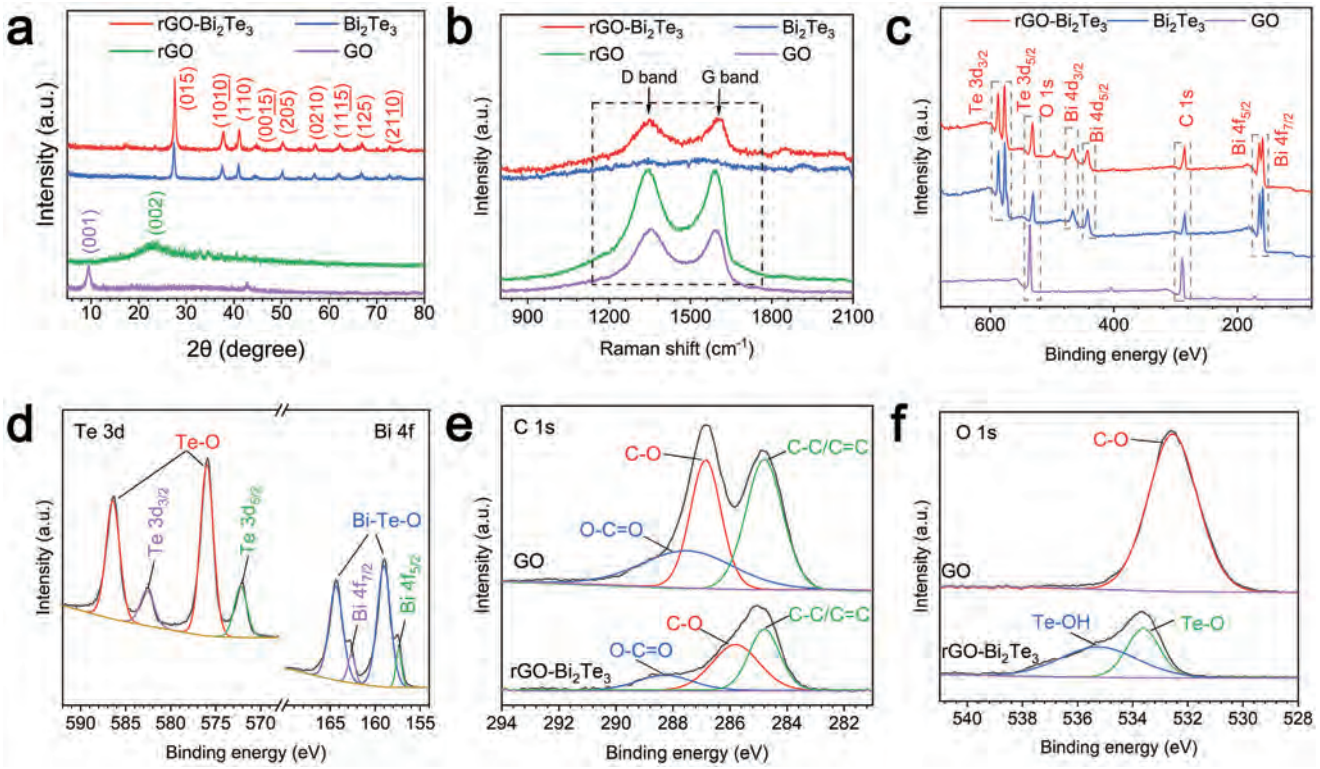

Figure 2. Structure characterization. a) XRD patterns. b) Raman spectra. c) XPS survey spectra. d) Te 3d and Bi 4f, e) C 1s, and f) O 1s of XPS spectra.

showed no obvious lattice fringes. The selective electron diffraction (SAED) pattern of rGO-Bi_2Te_3 (Figure 1e) indicated clear diffraction spots corresponding to (015), (101), (110), (116), and (205) planes, suggesting the high-crystalline characteristic of Bi_2Te_3 nanosheets. Correspondingly, the SAED pattern of rGO (Figure S2c, Supporting Information) demonstrated its amorphous state.[15] Both the EDS profile (Figure 1f) and the corresponding element mapping (Figure 1g) confirmed the uniform distribution of Te, Bi, C, and O elements. The atomic force microscope (AFM) images indicated that the thickness of Bi_2Te_3 nanosheets (≈33 nm, Figure 1h,i) was ≈4.5 nm thinner than that of rGO-Bi_2Te_3 nanosheets (≈37.5 nm, Figure 1j,k).

As shown in **Figure 2**a, all the X-ray powder diffraction (XRD) peaks of Bi_2Te_3 and rGO-Bi_2Te_3 were well matched with the characteristic peaks of Bi_2Te_3 crystal, including (015), (110), (1010), (205), (125), (1115), (0210), (0015), and (2110).[16] Besides, in the XRD pattern of rGO, the (002) diffraction peak reappeared, while the (001) diffraction peak in the original GO disappeared, proving the successful reduction of GO.[17] In Figure 2b, the Raman spectra of rGO and rGO-Bi_2Te_3 indicated two main characteristic peaks of rGO, which was ascribed to the *D*-Band at 1353 cm^{-1} and *G*-Band at 1592 cm^{-1}.[18] The *D*-band was caused by vibration of defects states in graphene sheets, and the *G*-band was the stretching vibration of C—C bonds during sp^2 C hybridization.[19] This result confirmed the close combination between rGO and Bi_2Te_3 successfully. The intensity ratio of I_D/I_G in rGO-Bi_2Te_3 (≈1.05) and rGO (≈1.0) was higher than that in GO (≈0.89), which further confirmed the successful reduction of GO.[20]

X-ray photoelectron spectroscopy (XPS) was employed to analyze the bonding interaction in GO, Bi_2Te_3, and rGO-Bi_2Te_3. As shown in Figure 2c, compared with GO and Bi_2Te_3, the survey spectra of the rGO-Bi_2Te_3 exhibited the obvious signals of four elements (Bi, Te, C, and O). Concretely, the main four peaks in the rGO-Bi_2Te_3 spectrum were classified as Bi $4f_{5/2}$ at 157.4, Bi $4f_{7/2}$ at 162.7, Te $3d_{5/2}$ at 572.4, and Te $3d_{3/2}$ at 582.7 eV, corresponding to Bi and Te.[21] The two relatively low peaks in 443 and 467 eV were Bi $4d_{5/2}$ and Bi $4d_{3/2}$, respectively. Notably, the narrow scan of Te 3d and Bi 4f (Figure 2d) disclosed the existence of Te—O and Bi—Te—O peaks. The former was located at 575.9 and 586.4 eV due to the surface oxidation of Te while the latter was at 158.9 and 164.4 eV.[22] The C 1s peaks (Figure 2e) in GO and rGO-Bi_2Te_3 were divided into three peaks, corresponding to 287.7 (O—C=O), 286.8 (C—O), and 284.8 eV (C—C/C=C). Besides, compared with GO group, the oxygen peaks (O—C=O and C—O) of rGO-Bi_2Te_3 sample had lower intensity and slight shift. The possible reasons might be the reduction of GO to rGO in rGO-Bi_2Te_3 and the interface interaction between Bi_2Te_3 and rGO. The O 1s spectra (Figure 2f) displayed only carbon—oxygen peaks (C—O) in GO, but tellurium oxygen peak (Te—O) and tellurium hydroxyl peak (Te—OH) at 533.6 and 535.3 eV in rGO-Bi_2Te_3, which might be related to the oxidation of tellurium atoms on the surface of rGO-Bi_2Te_3.[16c,23]

2.2. Photo-Thermoelectric Catalysis Performance and Mechanism

In **Figure 3**a, the temperature of Bi_2Te_3 and rGO-Bi_2Te_3 aqueous solutions recorded by a thermal camera increased to ≈50 and ≈55 °C (0.4 W cm^{-2}) upon near infrared (NIR) light

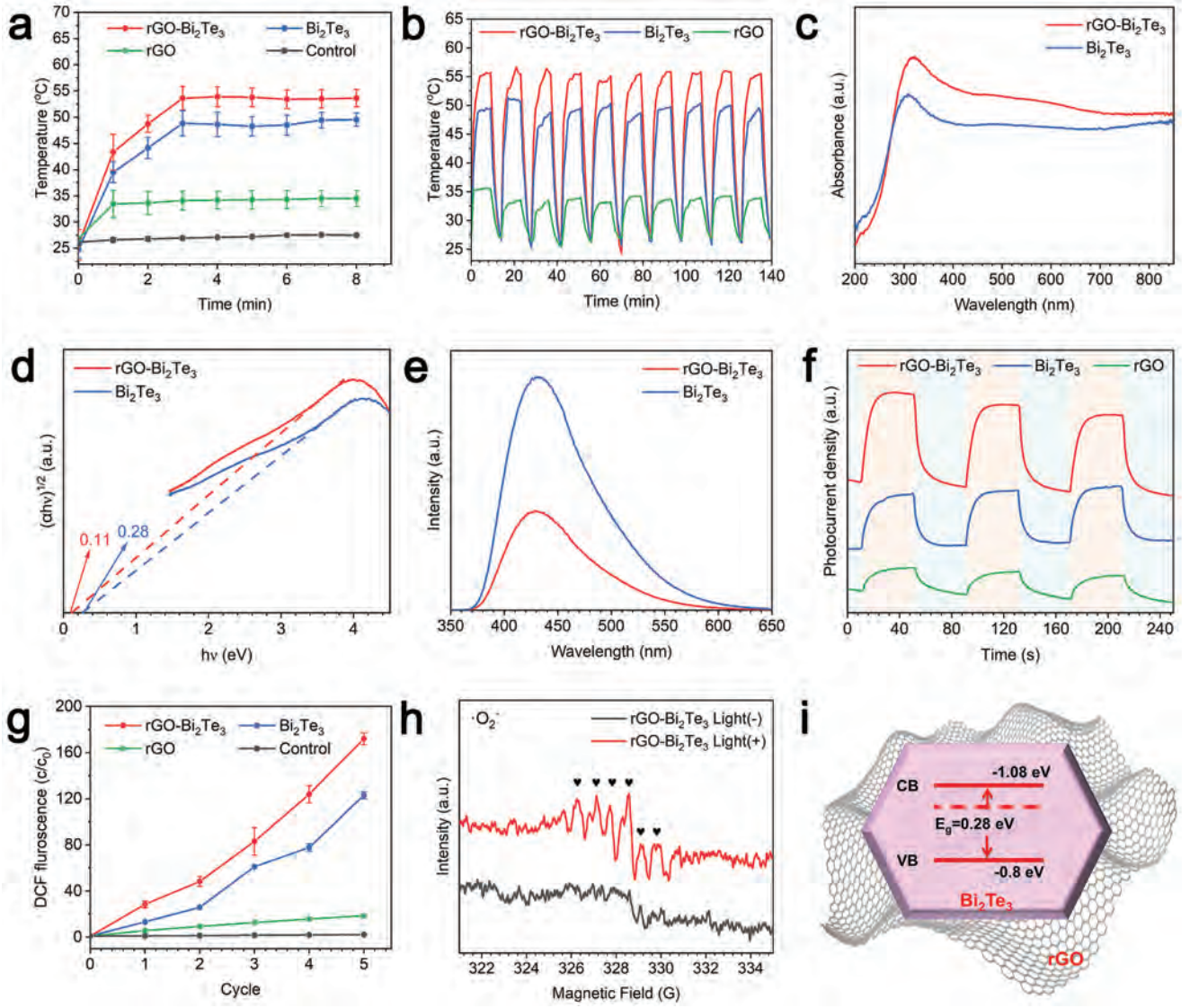

Figure 3. Optical characterization and optical property. a) Photothermal curves (n = 3). b) Photothermal stability curves. c) UV–vis-NIR spectrum. d) Band energy gap. e) PL spectra. f) Photocurrent spectra. g) ROS production with DCFH fluorescence probe (n = 3). h) ESR spectra of rGO-Bi_2Te_3 with and without light irradiation. i) Band structure alignments for rGO and Bi_2Te_3. Error bar indicates mean ± SD.

irradiation for 3 min, preliminarily confirming their good photothermal performance. Comparatively, the temperature of rGO rose slightly (<35 °C) by the same treatment. Compared with the photothermal conversion efficiency (η) of Bi_2Te_3 (41.35%), rGO-Bi_2Te_3 exhibited a higher value of 53.46%, confirming the combination of rGO and Bi_2Te_3 could significantly improve the photothermal performance of Bi_2Te_3.

As shown in Figure 3b, ten heating/cooling cycles under NIR laser irradiation obtained from rGO, Bi_2Te_3, and rGO-Bi_2Te_3 exhibited good stability. After 10 cycles, the photothermal temperature of rGO-Bi_2Te_3 could still keep 55 °C, suggesting the photostability of rGO-Bi_2Te_3. The UV–vis-NIR diffuse reflectance spectra shown in Figure 3c disclosed that rGO-Bi_2Te_3 had higher absorbance intensity than Bi_2Te_3. Besides, the certain red-shift peak of rGO-Bi_2Te_3 demonstrated that the interfacial interaction between rGO and Bi_2Te_3 could slightly affect the optical performance of rGO-Bi_2Te_3. According to the UV–vis diffuse reflectance spectra (Figure 3c), the calculated plots (Figure 3d) based on Kubelka-Munk function versus bandgap energy demonstrated that Bi_2Te_3 and rGO-Bi_2Te_3 had the bandgap of 0.28 and 0.11 eV, respectively,[24] which indicated that the photogenerated electron-hole pairs could be separated across the bandgap under NIR laser excitation. Thus, rGO-Bi_2Te_3 with a narrower bandgap might be a more appropriate NIR-responsive catalyst than Bi_2Te_3.

The photoluminescence (PL) spectra of rGO-Bi_2Te_3 and Bi_2Te_3 in Figure 3e displayed the characteristic peak at ≈430 nm. Compared with Bi_2Te_3, rGO-Bi_2Te_3 exhibited a lower PL intensity, suggesting an effective separation of photogenerated electron-hole pairs. Notably, the PL peak of rGO-Bi_2Te_3 had a slight blue-shift, confirming the certain interfacial interaction between rGO and Bi_2Te_3.

As shown in Figure 3f, the photocurrent response curves of rGO, Bi_2Te_3, and rGO-Bi_2Te_3 under 808 nm NIR light irradiation were measured by electrochemical workstation. Comparatively, rGO-Bi_2Te_3 exhibited the highest photocurrent density, further indicating the best performance of charges transfer and separation in rGO-Bi_2Te_3. However, the photocurrent density decreased slightly with time, which might be due to the slight shedding of the sample film with poor film-forming property. Additionally, the electrochemical impedance spectroscopy (EIS) in Figure S3 (Supporting Information) was employed to certify the internal resistance and interface charge transfer. Compared with Bi_2Te_3, rGO-Bi_2Te_3 with 808 nm light irradiation represented the smallest radius, reflecting its lower internal resistance and faster photogenerated charge transfer. Thermoelectric materials were often employed in cogeneration and noiseless cooling, which could convert the collected thermal energy into electricity.[25] Therefore, in a similar manner, it was expected that the temperature difference of thermoelectric materials induced a potential to generate ROS, enabling thermoelectric catalysis.

A commercial probe 2″,7″-dichlorodihydrofluorescein diacetate (DCFH-DA) was also used to detect the ROS production efficiency of Bi_2Te_3, rGO, and rGO-Bi_2Te_3 (Figure 3g). After several heating (808 nm light, 0.4 W cm^{-2}) and cooling cycles, the relative level of ROS production of rGO-Bi_2Te_3 was significantly higher than that of other groups. Besides, the above experiments were performed again with water bath (55 °C) heating instead of photothermal as a control, and the results showed that the production of ROS generated by rGO-Bi_2Te_3 was still much, which was ≈4/5 of that produced by photo-thermoelectric effect (Figure S4, Supporting Information). Correspondingly, the same operation was repeated in an ice-water bath and 808 nm light irradiation as a second control. Figure S5 (Supporting Information) showed that the ROS production of the rGO-Bi_2Te_3 group was ≈1/2 of that in experimental group. Hence, photo-thermoelectric catalysis to produce ROS should be the result of the combined effect of photothermal, photocatalysis, and thermoelectric catalysis. In Figure 3h, the electron spin resonance (ESR) spectrum showed no obvious signal was detected without NIR light irradiation, while the six characteristic signal peaks (marked by heart shape) of $\cdot O^{2-}$/5,5-Dimethyl-1-pyrroline N-oxide (DMPO) admixture was monitored under NIR light irradiation. Therefore, rGO-Bi_2Te_3-mediated photo-thermoelectric catalyst had the good ROS-generation ability. Under 808 nm light irradiation, 1,3-Diphenylisobenzofuran (DPBF) and terephthalic acid (TA) were used to detect $^1O_2$ and $\cdot OH$, respectively. The DPBF results in Figure S6a (Supporting Information) showed almost no $^1O_2$ was detected after 3 cycles of 808 nm light irradiation. The TA results in Figure S6b (Supporting Information) indicated there was no OH was produced during the light cycles. All above results suggested that rGO-Bi_2Te_3 nanosheets could efficiently generate $\cdot O^{2-}$ for catalysis by photo-thermoelectric under NIR laser irradiation.

Given the satisfactory photo-thermoelectric catalysis performance of rGO-Bi_2Te_3, its catalysis mechanism was further explored by characterizing the band structure. As revealed by the valence band (VB) XPS spectra (Figure S7, Supporting Information), the VB position of Bi_2Te_3 was located at –0.8 eV. The conduction band (CB) position was then calculated to be –1.08 eV by the equation (2),

$$E_{CB} = E_{VB} - E_g \tag{2}$$

where E_g, E_{CB} and E_{VB} represented the bandgap energy, CB potential, and VB potential, respectively.[26] It was very possible for Bi_2Te_3 to generate $\cdot O_2^-$ in thermodynamics due to the more negative CB potential than the redox potential of $O_2/\cdot O_2^-$ (–0.33 eV). Based on the above experimental and calculation results, the band structure could be schematically illustrated in Figure 3i.

2.3. Thermoelectric Performance and Mechanism

It could be observed that both Bi_2Te_3 and rGO-Bi_2Te_3 exhibited the temperature-dependent electrical conductivity (σ) (**Figure 4**a) and weighted carrier mobility (μ_w) (Figure 4b) in temperature range of 300 to 450 K, where σ values decreased with increasing temperature due to the decreased μ_w values. This phenomenon resulted from phonon scattering effect. Namely, when the temperature increased, the effect of phonon-scattering carriers inside Bi_2Te_3 and rGO-Bi_2Te_3 became more significant, causing the lower carrier mobility.[27] Concretely, σ value of rGO-Bi_2Te_3 (0.95×10^3 S cm^{-1}) at 300 K was significantly higher than that of Bi_2Te_3 (0.75×10^3 S cm^{-1}). Besides, μ_w value of rGO-Bi_2Te_3 (115.60 cm^2 V^{-1} s^{-1}) was largely improved compared with that of Bi_2Te_3 (76.82 cm^2 V^{-1} s^{-1}). According to the following equation (3):[28]

$$\sigma = en\mu_w \tag{3}$$

where e represents the electron charge and n is the carrier concentration. The above results implied the betterment in electrical conductivity of rGO-Bi_2Te_3 originated from its enhanced carrier mobility because rGO in the composite might provide an extra transport channel for electrons.

The increased Seebeck coefficient values of Bi_2Te_3 and rGO-Bi_2Te_3 with rising temperature were shown in Figure 4c. Notably, both of Bi_2Te_3 and rGO-Bi_2Te_3 exhibited negative Seebeck coefficient values and *n*-type thermoelectric properties, demonstrating that the charge transportation was mainly completed by electrons, not holes. The Seebeck coefficient absolute values of rGO-Bi_2Te_3 composite (93 to 115 μV K^{-1}) was significantly higher than that of Bi_2Te_3 (80 to 108 μV K^{-1}) from 300 to 450 K, indicating that the introduction of rGO was beneficial to the enhancement of Seebeck coefficient of *n*-type Bi_2Te_3. After introducing rGO, a large number of heterointerfaces between Bi_2Te_3 and rGO were formed. Meanwhile, due to the high energy barrier of the heterointerfaces, only relatively high-energy carriers could pass through the energy barrier of the heterointerfaces while the low-energy carriers were filtered out, which decreased the carrier concentration.[29] Additionally, Figure 4d also indicated that the carrier concentration of rGO-Bi_2Te_3 (5.14×10^{19} to 6.95×10^{19} cm^{-3}) was indeed lower than that of Bi_2Te_3 (6.09×10^{19} to 8.18×10^{19} cm^{-3}) from 300 to 450 K, and the carrier concentration of rGO-Bi_2Te_3 and Bi_2Te_3 increased with the rising temperature. This result also

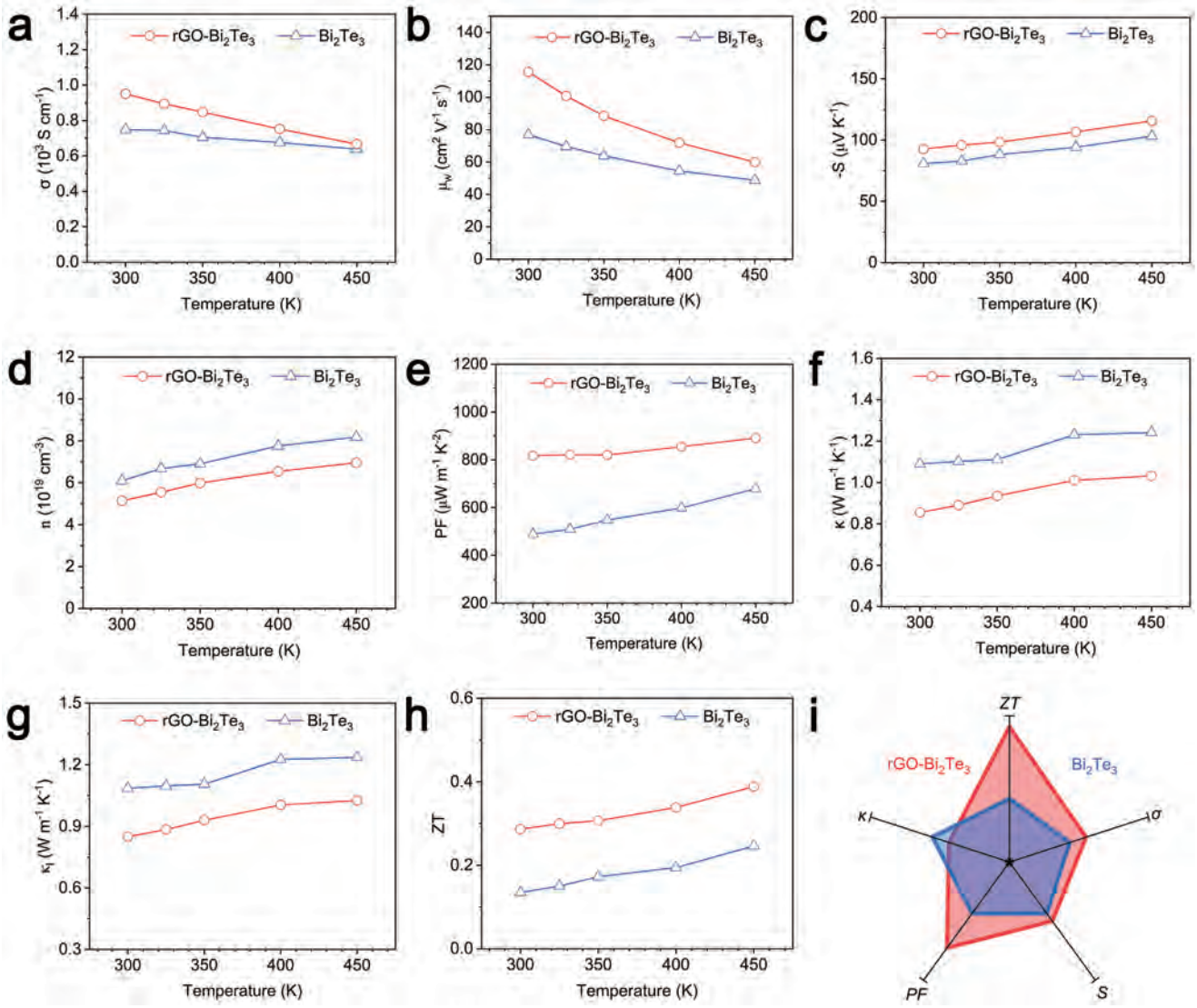

Figure 4. Thermoelectric properties of Bi_2Te_3 and rGO-Bi_2Te_3. a) Electrical conductivity. b) Weighted carrier mobility. c) Seebeck coefficient. d) Carrier concentration. e) Total thermal conductivity. f) Lattice thermal conductivity. g) Power factor. h) *ZT* values. i) The radar figure of five thermoelectric parameters.

confirmed the previous discussion about the σ issue. According to the Mott equation (4):[30]

$$S = -\frac{\pi^2 k_B^2 T}{3e}\left(\frac{dln\sigma}{dE}\right)|_{E=E_f} \quad (4)$$

where k_B is the Boltzmann constant, T represents the absolute temperature, e is the elementary charge, and E_f is the Fermi energy, the increased S of rGO-Bi_2Te_3 was likely due to the high σ.

In Figure 4e, the power factor (*PF*) values of Bi_2Te_3 and rGO-Bi_2Te_3 were calculated by the equation (5).

$$PF = S^2\sigma \quad (5)$$

The *PF* values of Bi_2Te_3 increased from 489 μW m^{-1} K^{-2} at 300 K to 679 μW m^{-1} K^{-2} at 450 K. Moreover, rGO-Bi_2Te_3 exhibited the highest *PF* value (891 μW m^{-1} K^{-2}) at 450 K by combining high σ with large S. The above results suggested that the combination of rGO with Bi_2Te_3 improved the σ and S of rGO-Bi_2Te_3, leading to an improvement in the overall electrical transport and thermoelectric performance of the material. The primary causes for the improved electrical transport performance were the extra transport channels provided by rGO for electrons and the influence of heterointerfaces between rGO and Bi_2Te_3.

In addition to electrical transport performance, thermal transport properties were also one of the most important parameters for evaluating the thermoelectric properties. In Figure 4f, the thermal conductivity (κ) value of Bi_2Te_3 fluctuated from 1.09 to 1.242 W m^{-1} K^{-1} in the rage of 300–450 K. Comparatively, the κ value of rGO-Bi_2Te_3 was increased from 0.855 to 1.032 W m^{-1} K^{-1}. Comparatively, the κ value of rGO-Bi_2Te_3 was decreased from 0.915 to 0.813 W m^{-1} K^{-1}. Generally, the total

thermal conductivity (κ) could be expressed as the sum of the lattice thermal conductivity (κ_l) and the electron thermal conductivity (κ_e), as shown in equation (6).

$$\kappa = \kappa_l + \kappa_e \tag{6}$$

In Figure S8 (Supporting Information) and Figure 4g, the κ_e value of both Bi_2Te_3 and rGO-Bi_2Te_3 was much smaller than the corresponding κ_l value. Thus, the κ value was dominated by κ_l under the phonon scattering mechanism. Since rGO was incorporated with Bi_2Te_3 to generate abundant heterointerfaces, which could effectively scatter phonons of relative wavelengths, thereby suppressing the growth of lattice thermal conductivity (κ_l).[31] Besides, the nanoscale voids existing in heterointerfaces between rGO and Bi_2Te_3 reduced the contact area and the interatomic forces on both sides, which led to an increase in the interfacial thermal resistance. Even the locations of perfect contact could also cause thermal resistance because of the differences in their intrinsic thermal transport properties and mismatch of phonon eigenmodes.[32] Therefore, the κ value of rGO-Bi_2Te_3 exhibited a certain reduction compared to Bi_2Te_3 owing to the increase in heterointerface thermal resistance of rGO-Bi_2Te_3.

According to the following equation (7),[7]

$$ZT = \frac{(PF)T}{\kappa} \tag{7}$$

The ZT of both Bi_2Te_3 and rGO-Bi_2Te_3 could be calculated to evaluate thermoelectric performance. As shown in Figure 4h, the ZT value of rGO-Bi_2Te_3 ranged from 0.29 to 0.39, which was higher than that of Bi_2Te_3 (0.13 to 0.25) at each measurement temperature point correspondingly. As shown in Figure 4i, the radar figure comprehensively reflected the five parameters (σ, S, PF, κ, and ZT) to compare the thermoelectric properties of rGO-Bi_2Te_3 and Bi_2Te_3. Overall, rGO-Bi_2Te_3 had higher thermoelectric parameters compared with Bi_2Te_3 except for thermal conductivity, while the κ value of rGO-Bi_2Te_3 was lower than that of Bi_2Te_3. Especially, the final ZT value of rGO-Bi_2Te_3 was 2.13 times higher than that of Bi_2Te_3. To sum up, the unique electronic characteristic with undisturbed electron transport determined the ultra-high carrier mobility of rGO, which provided extra carrier transport channels in rGO-Bi_2Te_3. Therefore, the electrical conductivity of rGO-Bi_2Te_3 was significantly improved by the enhanced carrier mobility. Besides, the abundant rGO-Bi_2Te_3 heterointerfaces could induce the phonon scattering effect, resulting in increasing interface thermal resistance and thus decreasing κ value. For rGO-Bi_2Te_3, the heterointerface-induced phonon scattering effect and extra carrier transport channels provided by rGO balanced the electrical transport and thermal transport properties, finally enhancing the thermoelectric performance.

2.4. Photo-Generated Charges Transfer and Photo-Thermoelectric Catalysis Mechanism

To further explore the spatial charge distribution of electron-hole pairs generated by rGO-Bi_2Te_3, surface potential analysis was performed using photo-assisted Kelvin probe force microscopy (KPFM).[33] As shown in **Figure 5**a–c and the corresponding distribution curves by Gaussian fitting in Figure 5d–f, the KPFM images of rGO-Bi_2Te_3 showed obvious variations with the laser turned on or off, demonstrating the charge transfer and separation in nanoscale. Specifically, the KPFM image of rGO-Bi_2Te_3 nanosheets under light irradiation (Figure 5c) became lower than that in dark (Figure 5b). Correspondingly, the average surface voltage of rGO-Bi_2Te_3 in light (260.99 mV in Figure 5e) was 26.4 mV lower than that in dark (234.59 mV in Figure 5f). The reduced contact potential difference (CPD) of rGO-Bi_2Te_3 indicated that the carriers with opposite polarity were separated from the rGO-Bi_2Te_3 surface after photothermal treatment, resulting in more electrons enrichment on the surface. Besides, the cross-line profiles (Figure 5g) at the same location also denoted that the surface potential in dark state (Line 2) was significantly higher than that in light state (Line 3). Then, the potential under light was subtracted from the potential in darkness as shown in Figure 5h. The increment of surface photo-thermovoltage at rGO-Bi_2Te_3 nanosheets was about −150 mV, which further verified the accumulation of electrons on rGO-Bi_2Te_3 surface. As schematically illustrated in Figure 5i, the spatial charge distribution on rGO-Bi_2Te_3 surface demonstrated that the photogenerated electrons and holes were separated into rGO and Bi_2Te_3, respectively. Moreover, the observed output voltage was a direct result of temperature-induced electron-hole separation in rGO-Bi_2Te_3.[34]

As schematically illustrated in **Figure 6**, the thermoelectric catalytic mechanism of rGO-Bi_2Te_3 for ROS generation was rationally divided into three steps. In the first period of heating, the excited photoelectrons and hot carriers of Bi_2Te_3 transferred from the VB to the CB of Bi_2Te_3 upon NIR laser irradiation. Next, the photoelectrons rushed from the hot side to the cold side, thus creating an internal electric field from the hot end to the cold end. Further, the band energy decreased at positive potential side and increased at negative potential side due to thermoelectric field. Both the CB and VB energy level were bent to keep up with this energy variation. Therefore, the electrons would migrate more easily from Bi_2Te_3 to rGO, which effectively improved the electron-hole separation efficiency, increased the free carrier concentration, and further promoted the ROS generation. In addition, the close contact between Bi_2Te_3 and rGO provided carrier transport channels, which was beneficial for more efficient thermoelectric catalysis. In the second constant temperature period, there were still many photoelectrons and hot carriers of Bi_2Te_3 leaped from VB into CB, and then migrated to rGO surface to form ROS. In the three period of cooling, the thermoelectric field induced by temperature differences accelerated the transfer and separation of accumulated charges. Then the free carriers would be captured by surrounding species to generate ROS.

In summary, the above three steps constituted a complete cycle, where the thermoelectric field and electron-conducting rGO played a key role in improving the electron-hole separation efficiency and thus generating abundant ROS. This efficient photo-thermoelectric catalysis platform for ROS generation had great potential in antibacterial applications.

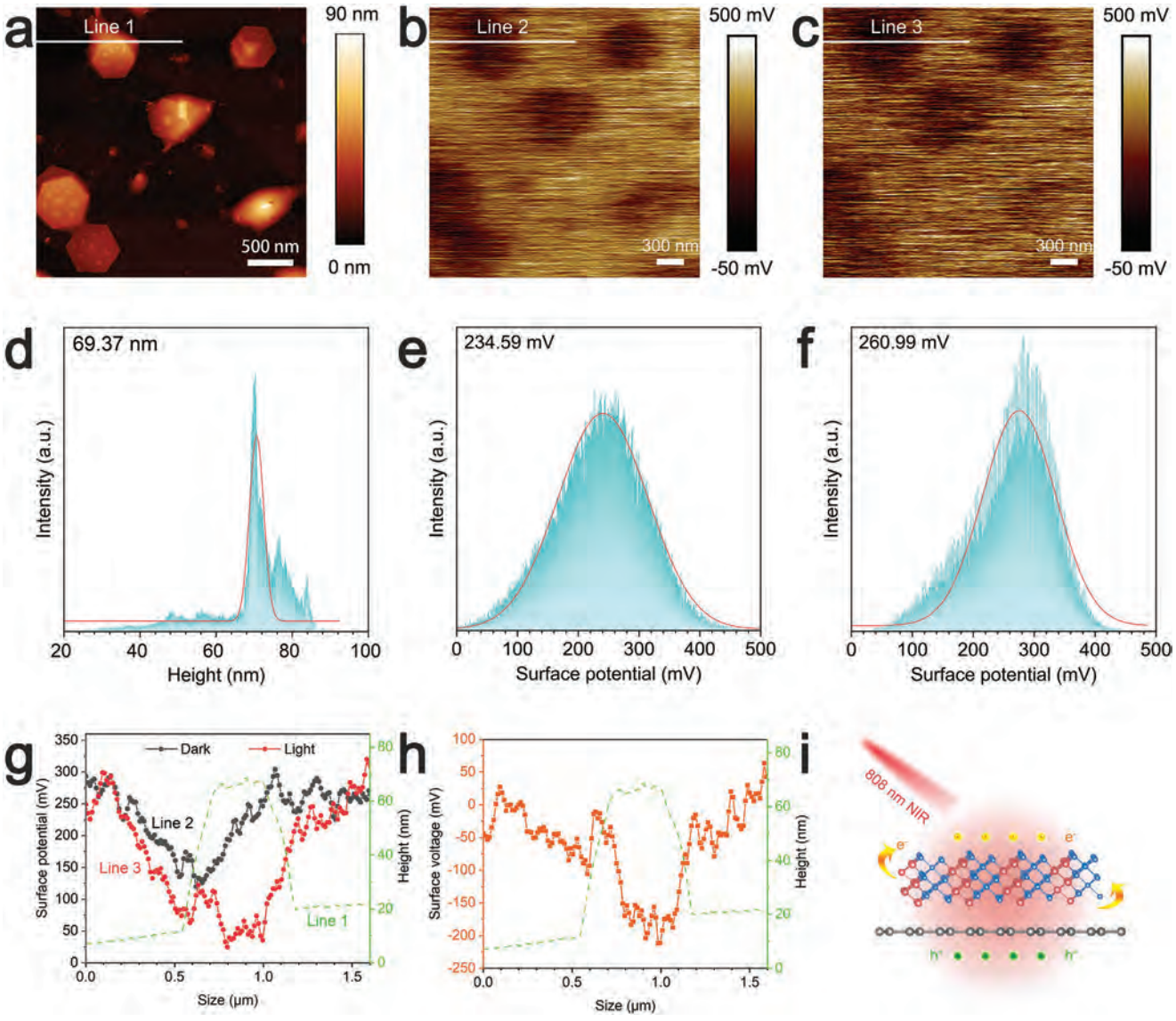

Figure 5. Photo-thermoelectric performance and catalytic mechanism. a) AFM topography image of rGO-Bi_2Te_3. b) c) KPFM images of rGO-Bi_2Te_3: b) in the dark and c) upon 808 nm illumination. d–f) Gaussian fitted statistical distribution corresponding to a–c). g) Contact potential difference (CPD) profiles of dark state (black line) and light state (red line) across the rGO-Bi_2Te_3 nanosheets. The green line is the corresponding thickness. h) Surface photovoltage (SPV) profile across the rGO-Bi_2Te_3 nanosheets by subtracting the potential under dark from that under 808 nm light irradiation. i) Schematic of electron migration of rGO-Bi_2Te_3 under 808 nm laser irradiation.

2.5. In Vitro Antibacterial and Biocompatibility Evaluation

The bacteria-killing function of the synthesized materials was achieved by its excellent photothermal and photo-thermoelectric catalytic capacity. As shown in Figure S9a,b (Supporting Information), when three heating and cooling cycles were controlled by NIR laser on and off, the number of bacterial colonies in the rGO-Bi_2Te_3 group was greatly reduced, and the antibacterial rate of rGO-Bi_2Te_3 (97.74 ± 2.35%) against *S. aureus* was higher than those of Bi_2Te_3 (62.23 ± 12.9%) and rGO (18.50 ± 10.6%). Meanwhile, the corresponding SEM images (Figure S10, Supporting Information) showed the bacteria treated by photothermal cycling in rGO-Bi_2Te_3 group were severely wrinkled and deformed, while the other groups showed relatively round and smooth spherical bacterial surface, suggesting the excellent bacteria-killing ability of the rGO-Bi_2Te_3 under 808 nm light irradiation.

Figure S11 (Supporting Information) indicated the cytocompatibility after 1 or 3 days of co-incubation with NIH-3T3 cells. Specifically, all samples exhibited no significant cytotoxicity (rGO-Bi_2Te_3, 87.27%, 95.26%; Bi_2Te_3, 83.30%, 93.71%, rGO, 89.97%, 97.45%; Ctrl, 100%, 100%) after 1 day and 3 days co-incubation with cells. Meanwhile, the fluorescent images (Figure S12, Supporting Information) of NIH-3T3 cells after co-cultured with different samples exhibited a large number of cells with good morphology, confirming no obvious cytotoxicity.

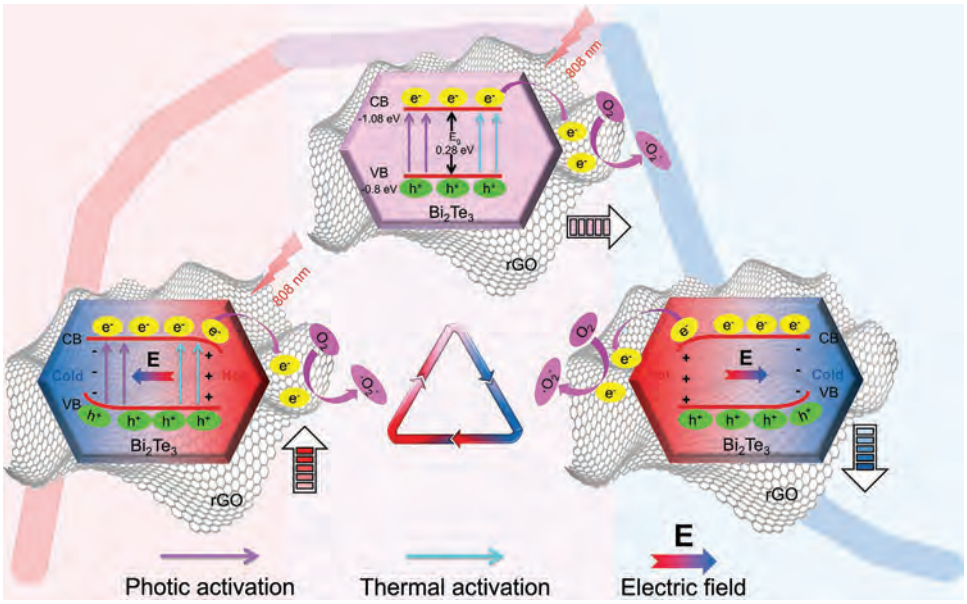

Figure 6. Schematic illustration of photo-thermoelectric catalysis mechanism.

2.6. Characterization of Electrospinning rGO-Bi_2Te_3@PU Membranes

Based on the excellent catalytic bactericidal performance of rGO-Bi_2Te_3 nanosheets, a bactericidal fabric was designed as a potential surgical dressing or other antibacterial products. As illustrated in **Figure 7**a, the fabrics with different proportions of rGO-Bi_2Te_3 were prepared by electrostatic spinning. The SEM images (Figure 7b) showed uniform and smooth fibers of PU, while more and more rGO-Bi_2Te_3 appeared in the fibers with the increasing content (10% rGO-Bi_2Te_3@PU, 30% rGO-Bi_2Te_3@PU, and 50% rGO-Bi_2Te_3@PU). Besides, the color of spinning membranes (the insets in Figure 7b) gradually became from white to black, preliminarily confirming the successful encapsulation of rGO-Bi_2Te_3 into PU spinning membranes. The TEM image (Figure S13a, Supporting Information) and corresponding EDS results (Figure S13b, Supporting Information) of 50% rGO-Bi_2Te_3@PU indicated rGO-Bi_2Te_3 was successfully spun into the nanofibers or on the fiber surfaces. Besides, The SEM images in Figure S13c,d (Supporting Information) showed more clearly that some rGO-Bi_2Te_3 nanosheets were wrapped or partially wrapped in PU nanofibers, and some rGO-Bi_2Te_3 nanosheets were loaded to the surface of nanofibers. The Fourier transform infrared spectrometer (FTIR) spectra in Figure S14 (Supporting Information) revealed that the characteristic peaks of rGO-Bi_2Te_3@PU and PU were similar, suggesting that the structure of the original PU fiber will not be changed after adding rGO-Bi_2Te_3. Next, the UV–vis-NIR diffuse reflectance spectra (Figure S15, Supporting Information) of different membranes (PU, 10%, 30%, and 50% rGO-Bi_2Te_3@PU) denoted the increasing absorption intensity in 200–850 nm. Especially, the absorption at 808 NIR light showed gradual increase trend with the content of rGO-Bi_2Te_3 increase.

Under NIR light (0.2 W cm^{-2}) irradiation, 50% rGO-Bi_2Te_3@PU heated up to ≈55 °C within 1 min while both 30% rGO-Bi_2Te_3@PU and 10% rGO-Bi_2Te_3@PU heated up to 48–51 °C. In contrast, pure PU only heated up and remained at ≈40 °C (Figure S16a, Supporting Information). Additionally, three heating and cooling cycles were realized by turning the laser on and off (Figure S16b, Supporting Information), demonstrating the photothermal stability of the fiber membranes.

Considering photothermal performance of membranes, 50% rGO-Bi_2Te_3@PU was chosen to detect ROS production by ESR (Figure S17, Supporting Information). Obviously, the signals of O^{2-}/DMPO was detected under NIR light illumination, indicating the ROS-generation ability of 50% rGO-Bi_2Te_3@PU membrane. Moreover, DCFH-DA fluorescence intensity in Figure S18 (Supporting Information) also revealed the highest ROS production generated by 50% rGO-Bi_2Te_3@PU. This might be affected by the photothermal temperature and the content of rGO-Bi_2Te_3. In Figure S19 (Supporting Information), the results of water contact angles of PU (≈139.1°), 10% rGO-Bi_2Te_3@PU (≈139.2°), 30% rGO-Bi_2Te_3@PU (≈137.3°) and 50% rGO-Bi_2Te_3@PU(≈141.3°) indicated they were hydrophobic, while the addition of rGO-Bi_2Te_3 did not affect the hydrophobicity of PU.

2.7. In Vitro Antibacterial and Biocompatibility Evaluation of rGO-Bi_2Te_3@PU Membranes

In Figure S20a,b (Supporting Information), compared with the other groups, the 50% rGO-Bi_2Te_3@PU membrane exhibited satisfactory bactericidal properties with an antibacterial rate of 91.88 ± 5.34% against *S. aureus* after NIR light cycle treatment. Subsequently, the antibacterial activity of rGO-Bi_2Te_3@PU membranes against MRSA was evaluated by spread plate method. As shown in Figure 7c,d, the MRSA counts in PU and rGO-Bi_2Te_3@PU groups had no significant difference in the dark. Under the NIR laser irradiation

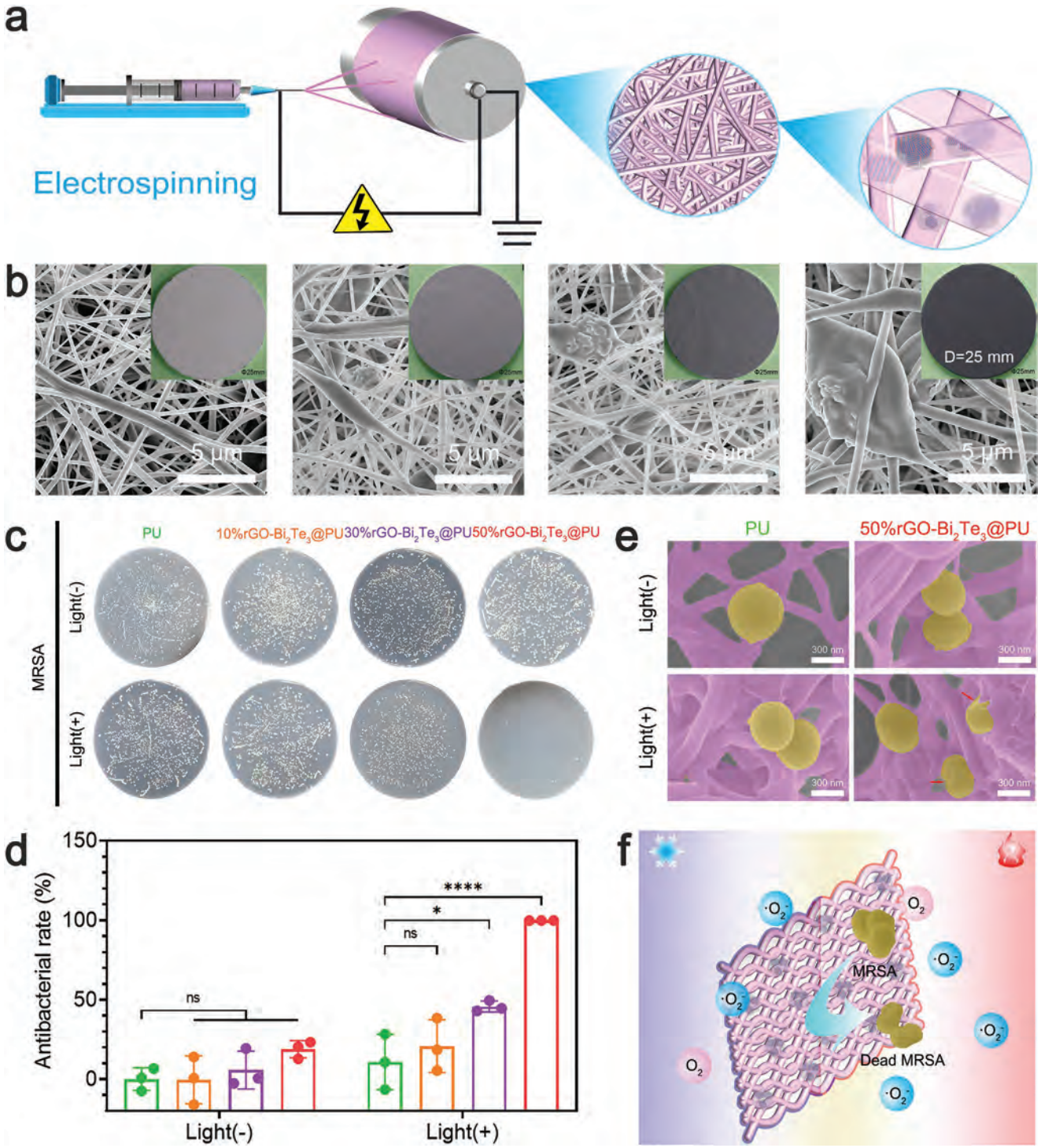

Figure 7. Characterization of sterilizable electrospinning films. a) Schematic illustration of the synthesis process of rGO-Bi_2Te_3@PU electrospun membranes. b) SEM images and optical photographs of spun films (PU, 10% rGO-Bi_2Te_3@PU, 30% rGO-Bi_2Te_3@PU and 50% rGO-Bi_2Te_3@PU). c) Spread plate of MRSA. d) SEM morphologies of MRSA. e) Antibacterial efficiency. f) Schematic illustration of antibacterial mechanism. Individual data points ($n = 3$ biologically independent samples) and error bar indicates mean ± SD. Statistical differences were analyzed by two-way ANOVA with Sidak's post hoc test (*$p < 0.05$, ****$p < 0.0001$, *ns* = no significant difference).

(0.2 W cm^{-2}), 50% rGO-Bi_2Te_3@PU exhibited high antibacterial rate (99.78 ± 0.03%). Correspondingly, the antibacterial rates of 30% rGO-Bi_2Te_3@PU, 10% rGO-Bi_2Te_3@PU, and PU were 62.84 ± 2.81%, 15.19 ± 13.53%, and 4.03 ± 14.21%, respectively. In order to clarify the antibacterial mechanism, the bacterial morphologies of PU and 50% rGO-Bi_2Te_3@PU spinning

membranes were examined. As shown in Figure 7e, MRSA in PU and 50% rGO-Bi_2Te_3@PU groups in the dark displayed a typical spherical shape with smooth surface without damage. In contrast, the MRSA bacteria on 50% rGO-Bi_2Te_3@PU became corrugated and distorted or even partly lysed.

Accordingly, the antibacterial mechanism was proposed as follows (Figure 7f). First, under 808 nm NIR light irradiation, the rGO-Bi_2Te_3@PU absorbed and converted light into heat. Then, the heat energy was used as a temperature source, along with an additional set of hot and cold cycling processes, to provide a temperature differential drive for the rGO-Bi_2Te_3 photothermoelectric catalyst. Subsequently, both the thermoelectric and photocatalytic effects were triggered to produce ROS, which destroyed the bacterial membrane structure and oxidized the internal proteins. In summary, ROS and heat acted synergistically on bacteria to further accelerate bacterial death.

Figure S21a (Supporting Information) indicated the cytocompatibility after 1 or 3 days of co-incubation with NIH-3T3 cells. Specifically, all spinning membranes exhibited high cell viability (PU, 91.28%; 10% rGO-Bi_2Te_3@PU, 114.53%, 30% rGO-Bi_2Te_3@PU, 89.8%; 50% rGO-Bi_2Te_3@PU, 125.17%) after 1 day co-incubation with cells, which may be due to the influence of the surface morphology of spinning fibers. In Figure S21b (Supporting Information), the hemolytic percentage (<5%) of all rGO-Bi_2Te_3@PU spinning membranes were much lower than the positive control group (1% Triton X-100 is a surfactant that can destroy cell membranes), indicating good blood compatibility. The above results disclosed the excellent biocompatibility of rGO-Bi_2Te_3@PU membranes.

2.8. In Vivo MRSA Wound Infection Model

Since the rGO-Bi_2Te_3@PU spinning membranes possessed excellent in vitro antibacterial ability and good biocompatibility, MRSA-infected animal wound model was designed to evaluate the therapeutic effect of 50% rGO-Bi_2Te_3@PU in vivo (**Figure 8**a). The synergistic effect of photothermal and

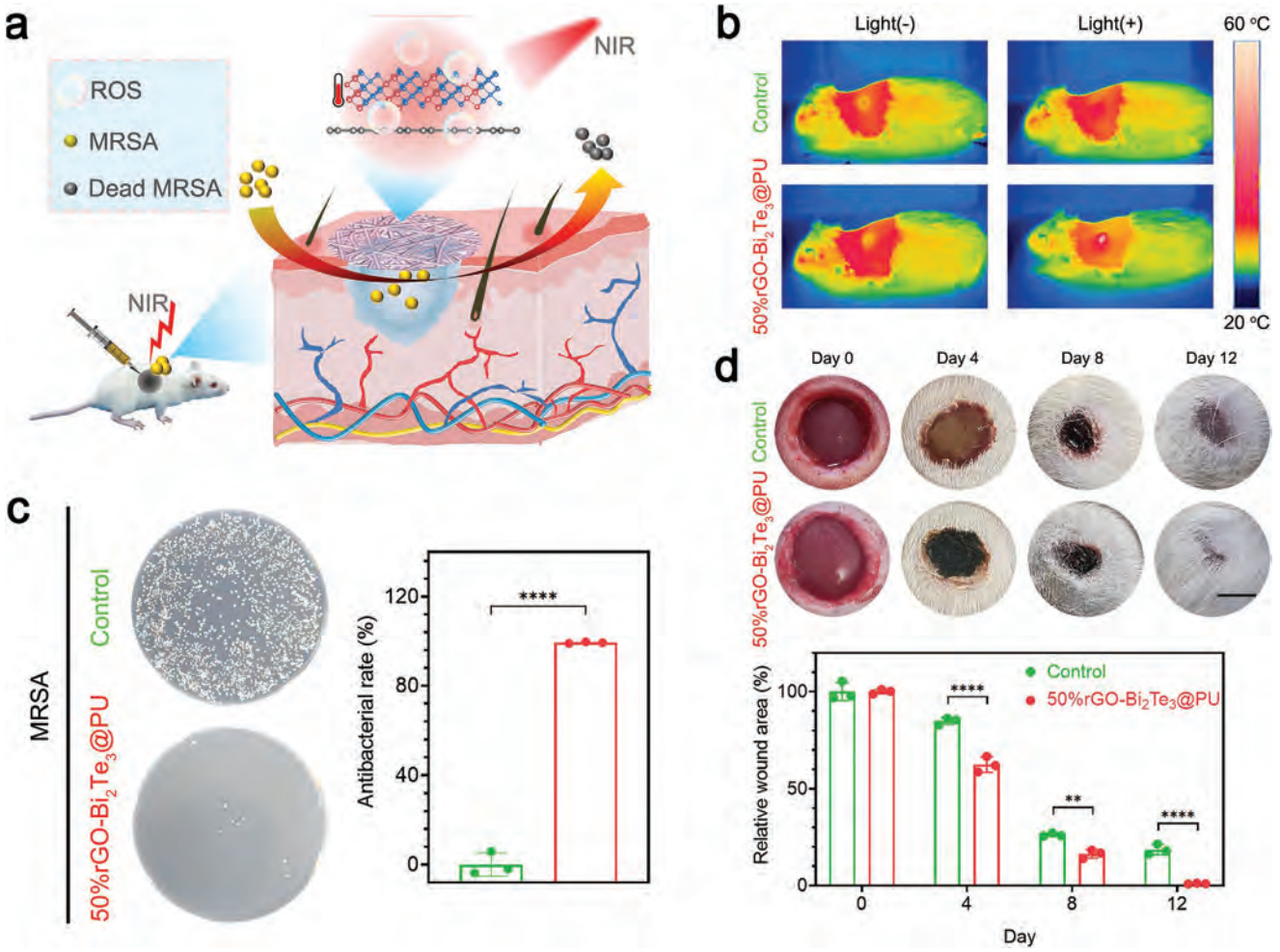

Figure 8. In vivo therapy for MRSA wound infection. a) Mechanism of therapy for MRSA wound infections in vivo. b) Photothermal images of control and 50% rGO-Bi_2Te_3@PU groups during NIR irradiation. c) Quantitative assessment of bacterial counts in wounds by spread plate method and corresponding viability of MRSA. d) Representative photographs of the wound healing process and corresponding quantitative analysis of wounds over time (scale bars = 5 mm). Individual data points ($n = 3$ biologically independent samples) and error bar indicates mean ± SD. Statistical differences were analyzed by two-way ANOVA with Sidak's post hoc test or a two-tailed Student's *t*-test (**$p < 0.01$, ****$p < 0.0001$).

photo-thermoelectric catalysis of 50% rGO-Bi_2Te_3@PU was utilized to kill MRSA in wounds. MRSA-infected rats were divided into two groups: control PU group and experimental 50% rGO-Bi_2Te_3@PU group. All rat wounds were treated with 808 nm NIR light in a heating and cooling cycle. As shown in Figure 8b, the real-time temperature of the wounds before and after illumination was recorded by thermal imager. Without light, the wound temperature of rats in the control group and the experimental group was about ≈35 °C. After 1 min of illumination, the wound temperature in the 50% rGO-Bi_2Te_3@PU group increased to ≈55 °C, while that in the PU group remained at ≈40 °C. Then, the bacterial counts in MRSA-infected wounds were quantified by spread plate method to evaluate the antibacterial ability of the spinning membranes. Obviously, 50% rGO-Bi_2Te_3@PU group exhibited superior bactericidal efficacy (antibacterial rate of 99.35 ± 0.29%) against MRSA compared with the control group, which was well consistent with in vitro antibacterial results (Figure 8c). The representative images in wound healing process in Figure 8d demonstrated that a certain degree of suppuration occurred in the control group on Day 4, while the wound healing speed of the rGO-Bi_2Te_3@PU group was significantly faster than that of the control group. This was also confirmed by quantitative analysis of wounds over time.

Hematoxylin and eosin (H&E) staining of the wound tissues (Figure S22, Supporting Information) indicated that a mass of neutrophils were observed in the control group, suggesting a more severe bacterial infection at the wounds. On the contrary, the degree of bacterial infection in the experimental group was significantly reduced, indicating the effective bactericidal ability and alleviated inflammation of 50% rGO-Bi_2Te_3@PU spinning membrane in vivo. In addition, Masson's trichrome staining and Sirius red staining were conducted on infected wound tissues on Day 12 to evaluate the new collagen deposition level (Figure S23a, Supporting Information). The collagen deposition level of the 50% rGO-Bi_2Te_3@PU group (blue region and red region) was higher than that of the control group, suggesting 50% rGO-Bi_2Te_3@PU had good ability of promoting wound tissue recovery, which was further supported by the quantitative measurements of the relative area of collagen in Masson trichromatic staining and Sirius red staining (Figure S23b,c, Supporting Information).

Hematology tests and histological analysis were performed to assess the biosafety of the electrospinning membranes in vivo. As shown in Figure S24 (Supporting Information), there were no significant differences in hematology analysis (WBC, RBC, HGB, HCT, MCV, MCH, and RDW) between the control group and the rGO-Bi_2Te_3@PU group. All the hematology analysis of the control group and the experimental group were within the standard normal range. In addition, the main organs (heart, liver, spleen, lung, and kidney) of rats on Day 12 were analyzed by H&E staining (Figure S25, Supporting Information). There was no evidence of organ damage and no significant difference between the two groups. The above results indicated that the spinning membranes had excellent biosafety in vivo.

3. Conclusion

In this work, Bi_2Te_3 nanosheets were in situ grown on rGO to generate an efficient photo-thermoelectric catalyst of rGO-Bi_2Te_3, where the heterointerface-induced phonon scattering effect and extra carrier transport channels provided by rGO improve thermoelectric performance (2.13 times) by increasing electrical conductivity, Seebeck coefficient, and decreasing thermal conductivity. In photothermy-driven thermoelectric catalysis, the excited photogenerated electrons and hot carriers transitioned from the VB to CB of Bi_2Te_3, and then the carriers more easily migrated to the surface of rGO and generate ROS under light-heat-electric conversion under NIR laser irradiation. Their heterointerfaces could effectively promote charges transfer and separation, thereby inhibiting electron-hole recombination to improve the catalytic efficiency. Additionally, rGO-Bi_2Te_3 nanosheets were integrated into PU fibers by electrospinning process to form spinning membranes. The functional spinning membrane was used in a MRSA-infected wound healing model, showing excellent disinfection performance, accelerated tissue repair, and reliable biosafety. This work provides an insight into heterointerface design in photothermoelectric catalysis.

4. Experimental Section

Materials: Bismuth nitrate pentahydrate ($Bi(NO_3)_3{\cdot}5H_2O$), polyvinyl pyrrolidone (PVP, K30), and sodium hydroxide (NaOH) were purchased from Sinopharm Chemical Reagent Co. (China). Sodium tellurite (Na_2TeO_3, 99.9%), N,N-dimethylformamide (DMF), and tetrahydrofuran (THF) were purchased from Aladdin (Shanghai, China). Ethylene Glycol (EG, 98%) was purchased from Macklin Biochemical Co., Ltd. (Shanghai, China). Graphene oxide (GO) was purchased from Turing Evolution Technology Co., Ltd. (Shenzhen, China). Isopropyl alcohol (C_3H_8O) and acetone were purchased from Kermel Chemical Reagent Co., Ltd. (Tianjin, China). Polyurethane (PU, 90A) was purchased from Ucalery Technology Development Co., Ltd. (Beijing, China). All chemicals were used directly without further purification.

Synthesis of Bi_2Te_3 and rGO-Bi_2Te_3: For the synthesis of the Bi_2Te_3 nanosheets, Na_2TeO_3 (0.133 g) and NaOH (0.32 g) were dissolved in 10 mL EG to obtain solution A. $Bi(NO_3)_3{\cdot}5H_2O$ (0.194 g) and PVP (0.4446 g) were added into another 10 mL of EG to yield solution B. After magnetic stirring for 30 min, the solution A was injected into B followed by vigorous stirring until the solution was homogeneous. After that, the mixture was placed in the water bath at 60 °C for 30 min. And then, the mixed solution was transferred into a 50 mL Teflon-lined autoclave to maintain 190 °C for 3 h. After the reaction, the resulting material was collected by centrifugation, washed three times with isopropyl alcohol and acetone. Finally, the Bi_2Te_3 nanosheets were dispersed in an isopropyl alcohol solution and used for further experiments.[16a]

For the preparation of the rGO-Bi_2Te_3 nanosheets, 2.50 mg of GO was dissolved in 10 mL EG by sonicating for 4 h. Then, the GO solution was added into the solution B. After stirring evenly, solution A was added to the above solution and continued stirring. The mixture was placed in the water bath at 60 °C for 30 min. And then, the mixed solution was transferred into a 50 mL Teflon-lined autoclave to maintain 190 °C for 3 h. Centrifugation and washing steps were the same as the above-mentioned method of Bi_2Te_3.

Fabrication of rGO-Bi_2Te_3@PU Nanofibers: PU (10 wt.%) was dissolved in a mixture of THF and DMF (v/v, 3:1) and stirred for 2 h. An appropriate amount of rGO-Bi_2Te_3 nanosheets (0, 10, 30, or 50 wt.% relative to the polymer mass) were added to the above solution and stirred to obtain a homogeneous and viscous solution. Then, the sol was collected into a hypodermic syringe (5 mL) for electrospinning. The parameters were as follows: spinning voltage: 13 kV; air gap distance: 15 cm; inner diameter of spinneret: 0.7 mm; floe rate of the solution: 0.1 mm min^{-1}; temperature: 26 °C. These samples were named as PU,

10% rGO-Bi_2Te_3@PU, 30% rGO-Bi_2Te_3@PU, and 50% rGO-Bi_2Te_3@PU, respectively.

Characterization: The morphologies of all the samples were observed by SEM (s4800, Hitachi) and TEM (JEM-2100 F, JEOL) equipped with EDS. The thickness of samples was measured by AFM (Agilent 5500; Bruker Dimension Icon). The crystalline structure, chemical structure, and surface compositions were analyzed by XRD (D8 Advance, Germany), FTIR (Nicolet IS10, United States), and XPS (ThermoFisher Scientific 250Xi, USA), respectively. The Raman spectra were recorded by using a DXR Raman microscope (Themo Scientific) equipped with a DXR 532 nm laser. The UV–vis-NIR absorption was measured by a UV–vis spectrophotometer (UV-2700, Shimadzu). PL spectra were measured by fluorescence spectrophotometer (Fluorolog-3, USA). Amplitude modulated Kelvin probe force microscopy (AM-KPFM) equipped with a NIR laser was employed to monitor the surface potential distribution of the samples.

Photothermal Performance Measurements: The temperature trends of the Control group, rGO, Bi_2Te_3, and rGO-Bi_2Te_3 (5 mg mL^{-1}) solution were measured under NIR laser (0.4 W cm^{-2}) for 8 min. The control group was pure deionized water. Besides, the electrospinning membrane samples were cut into discs with $\varphi = 10$ mm and irradiated with NIR laser (0.2 W cm^{-2}) for 6 min. All samples achieved a heating-cooling process under a light-dark cycle. The temperature of the samples was recorded using real-time thermal imaging monitored by a FLIR thermal camera (FLIRE64501, Estonia). The experiment was repeated three times.

The photothermal conversion efficiency (η) of rGO-Bi_2Te_3 can be calculated by equation (8).

$$\eta = \frac{hS(T_{max} - T_0) - Q_0}{I(1 - 10^{-A})} \tag{8}$$

where η represents the heat transfer coefficient, h is the heat transfer coefficient, S indicates the heated area, T_{max} is the highest temperature and T_0 is the initial temperature, Q_0 represents the heating absorption energy of container, I is the laser power, and A is the absorbance at NIR laser.

If the heat input of the system is equal to the heat output (equation (9)),

$$hS = \frac{\sum_i m_i C_{p,i}}{\tau_S} \approx \frac{m_{H_2O} C_{H_2O}}{\tau_S} \tag{9}$$

where m_{H_2O} represents the weight of water, C_{H_2O} denotes the specific heat capacity of water, and τ_S is the time constant. During the cooling period (equation (10)),

$$t = -\tau_S ln\theta = -\tau_S ln\frac{T - T_0}{T_{max} - T_0} \tag{10}$$

where T represents the real-time temperature. Thus, τ_S can be calculated using the linear regression curve.

Photocatalytic Evaluation: The photoelectrochemical performance of the samples was measured by an electrochemical workstation (CHI660E) equipped with a standard three-electrode system. In this measurement system, Ag/AgCl electrode, platinum plate, and samples were used as the reference electrode, counter electrode, and the working electrode, respectively. The electrolyte was a 0.1 M Na_2SO_4 solution. The solid sample (4 mg) was dissolved in a mixture (1 mL) of water and ethanol (v/v, 7:3). Then, 80 µL Nafion was added to the solution. Finally, 150 µL mixed solution was dropped on fluoride-tin oxide conductor glass to form a uniform membrane. Photoelectrochemical performance tests were performed with and without NIR light.

ROS Measurement: The ROS production of the samples was detected by a standard Reactive Oxygen Species Assay Kit. The principle was that microplate reader could detect the fluorescence produced by the reaction of 2″,7″-dichlorofluorescein (DCF) and ROS. The samples were subjected to different conditions: a) 808 nm light irradiation (0.4 W cm^{-2}); b) 55 °C water bath; c) 808 nm light irradiation (0.4 W cm^{-2}) in ice-water bath. The mixture of the sample and detection agent after each cycle treatment was placed on a microplate reader to detect the fluorescence intensity to measure ROS yield.

The ROS species of the samples were investigated via ESR (JES-FA200) spectroscopy. A certain amount of sample solution was mixed with capture agent DMPO, then irradiated with 808 nm light (0.4 or 0.2 W cm^{-2}), and finally the ESR spectrum of the solution was measured by capillary method.

DPBF was used to detect whether $^1O_2$ was produced after light irradiation. The absorption curves of DPBF at 350–450 nm were detected by microplate reader. TA was used to detect whether·OH was produced during light cycles. Then the yield of OH was verified by measuring the fluorescence intensity with a microplate reader.

Thermoelectric Evaluation: The electrical conductivity and Seebeck coefficient were tested at the same time with the Beijing Cryoall CTA-3 electrical performance testing system from room temperature to 450 K. The testing principle of electrical conductivity was the four-electrode method. The sample was placed vertically between the upper and lower electrodes. When a small current (I) was passed into the sample through the dual electrodes, the voltage (dE) could be measured by using the two negative electrodes (Pt electrodes) of the two pairs of thermocouples as wires. UI testing needed to be done in advance to ensure the verticality of the test and improve the stability of the test data. UI test was performed by gradually increasing from −3.7 to +3.7 mA at a fixed temperature, and to test voltage changes. The test started after the slope >0.99999. Finally, the resistivity could be calculated at different temperatures according to the ratio of UI.

The holder with heater created a certain temperature difference between the two ends of the sample to measure Seebeck coefficient. After the temperature difference was stable, the temperature T1 and T2 of the upper and lower parts were obtained by two pairs of thermocouples closed to the sample surface. The sample thermoelectric potential (dV) was measured by the negative electrodes (Pt electrodes) of thermocouples. Finally, S was obtained by calculation. Before the test, the sample was sprayed with boron nitride (except for the contact with the electrode and the thermocouple) to reduce the equipment pollution due to element volatilization.

The thermal diffusivity was measured with a Netzsch LFA-457 laser thermal conductivity meter and analyzed using the Cowan model with pulse correction. Before the test, graphite was sprayed on both sides of sample to enhance the light energy absorption on sample surface and enhance the sample infrared emissivity. Thermal conductivity was calculated by equation (11)

$$\kappa = \alpha \rho C_p \tag{11}$$

where α, ρ, C_p are thermal diffusivity, density, and specific heat capacity, respectively. The specific heat capacity was measured by Differential Scanning Calorimetry (DSC). Table S1 (Supporting Information) provided relevant data measured by DSC.

The weighted mobility (electron mobility weighted by the density of electronic states) was calculated using a combined Seebeck coefficient and resistivity measurement system according to equation (12) in the previous literature.[35]

$$\mu_w = 331 \frac{cm^2}{V_S} \left[\frac{(m\Omega)cm}{\rho}\right] \left(\frac{T}{300\,K}\right)^{\frac{3}{2}} \left\{\frac{exp\left(\frac{|S|}{k_B/e} - 2\right)}{1 + exp\left[-5\left(\frac{|S|}{k_B/e} - 1\right)\right]}\right\} + \frac{\frac{3}{\pi^2}\frac{|S|}{k_B/e}}{1 + exp\left[5\left(\frac{|S|}{k_B/e} - 1\right)\right]} \tag{12}$$

μ_w is the weighted mobility, ρ is the electrical resistivity measured in mΩ cm, T is the absolute temperature in K, S is the Seebeck coefficient, and $k_B/e = 86.3\ \mu V\ K^{-1}$.

The electrical thermal conductivity was estimated through the Wiedemann-Franz law (equation (13)),

$$\kappa_e = L\sigma T \tag{13}$$

where L was Lorenz.

A satisfactory approximate L value was obtained by this equation (14):[36]

$$L = 1.5 + exp\left(-\frac{|S|}{116}\right) \tag{14}$$

Therefore, the lattice thermal conductivity could be calculated by equation (15):

$$\kappa_l = \kappa - \kappa_e \tag{15}$$

In Vitro Antibacterial Experiments: The antibacterial activity of the samples against MRSA (ATCC 43 300) was quantitatively using the spread-plate method. After culturing MRSA in an incubating medium for ≈24 h, MRSA suspensions were diluted to $\approx 10^7$ CFU mL^{-1} in LB medium for subsequent experiments.

The antibacterial test was performed under NIR laser irradiation for heating and cooling cycle three times. In each cycle, the bacterial suspension containing the samples was allowed to warming up (T < 55 °C) by light irradiation for 5 min, and then was returned to room temperature for 5 min. At the same time, groups without thermal cycling or without light were set as controls. After appropriate dilution, bacteria suspension were plated on agar plates and cultured at 37 °C for 20 h. For the antibacterial activity of electrospinning nanofibers, the antibacterial methods were generally the same as described above. The diluted bacterial suspension was dropped on the membranes. The PU group was used as the control group. The antibacterial rate was calculated by measuring the number of bacterial colonies on the plate by equation (16):

$$\text{Antibacterial efficiency}(\%) = \frac{A-B}{A} * 100\% \tag{16}$$

where A is the average number of bacteria colonies in the control group (CFU/sample), and B is the average number of bacteria colonies in the experimental group (CFU/sample).

For bacterial SEM observation, the bacteria were treated with or without NIR laser and fixed with a 2.5% glutaraldehyde solution for 40 min. Then, the samples were dehydrated with different concentrations of ethanol solutions (10, 30, 50, 70, 90, and 100%) in turn, with each step taking 15 min. The bacterial morphology was observed by SEM after drying.

In Vitro Cytocompatibility Evaluation: The NIH-3T3 cells (mouse embryonic fibroblast cell line) were cultured in the growth medium containing 10% (v/v) fetal bovine serum and 1% penicillin-streptomycin solution) in a humidified atmosphere with 5% CO_2 at 37 °C.

The cell viability and proliferation on the electrospinning membranes were evaluated by the water-soluble tetrazole (2-(2-methoxy-4nitrobenzene)-3-(4-nitrobenzene)-5-(2,4-disulfobenzene)-2H-tetrazole monosodium salt) (CCK-8) method according to manufacturer instruction. Cells were co-cultured with different spinning samples after 1 day and 3 days. Finally, cell viability can be characterized by measuring absorbance at 450 nm with a microplate reader.

Cell cytotoxicity was assessed via Thiazolyl Blue Tetrazolium Bromide (MTT) method with NIH-3T3 cells. The samples were immersed in cell medium for 1 and 3 days, and the leaching solution was placed in well plates with cells. The well plate was incubated at 37 °C in a 5% carbon dioxide (CO_2) incubator for 1 and 3 days. After incubation, MTT solution and dimethyl sulfoxide (DMSO) were added to the well plate in turn and treated accordingly. Finally, the optical density of the supernatant was measured at 490 nm by a microplate reader.

Fluorescent Morphology: After the cells were co-cultured with the samples for a period of time, the samples were washed three times with phosphate buffered saline (PBS) and fixed in 4% formaldehyde for 10 min at room temperature, and then rinsed with PBS. Afterward, the samples were stained with fluorescein isothiocyanate (FITC) for 30 min in the dark, rinsed three times with PBS, and then stained with propidium iodide (DAPI) for 30 s and rinsed three times with PBS. FITC-stained cytoskeletal actin (green fluorescence) and DAPI-stained nuclei (blue fluorescence) were photographed by fluorescence microscopy.

Hemolysis Evaluation of Electrospinning Nanofibers: First, 5 mL of fresh rat blood was taken, diluted with 50 mL of PBS solution, and centrifuged in the mixed solution to obtain red blood cells (RBCs). Then, the erythrocytes were washed three times with PBS and resuspended in 20 mL PBS solution. An equal amount of diluted RBCs was added to the well plate where the spinning membrane samples had been placed. The plate was incubated at 37 °C for 4 h. After centrifugation, the absorbance of the supernatant was measured at 405 nm. A positive control (100% lysis) was prepared by treating RBCs with 1% Triton X-100. The hemolysis percentage was calculated by comparing the absorbance values of these samples with the positive control.

Rat Cutaneous MRSA Wound Infection Model: All the animal experiments were complied with the guidelines of the Tianjin Medical Experimental Animal Care, and animal protocols were approved by the Institutional Animal Care and Use Committee of Yi Shengyuan Gene Technology (Tianjin) Co., Ltd. (protocol number YSY-DWLL-2022054). All animals were kept and utilized in accordance with the Animal Management Rules of the Ministry of Health of the People's Republic of China and the Guidelines for the Care and Use of Laboratory Animals of China.

Twelve Sprague-Dawley male rats were randomly divided into two groups (n = six per group) that control and 50% rGO-Bi_2Te_3@PU groups. The backs of the rats were depilated and sterilized after anesthesia, and then two symmetrical circular wounds with a diameter of 10 mm were made on the back of each rat. Next, each wound from each group was infected with a MRSA dose of 10^7 CFU per wound. Based on the excellent antibacterial properties of 50% rGO-Bi_2Te_3@PU membrane with the antibacterial rate of 91.88 ± 5.34% against *S. aureus* and 99.78 ± 0.03% against MRSA after NIR light three cycles treatment in vitro, the antibacterial test conditions in vivo were determined as three cycles. The prepared electrospinning membranes (PU and 50% rGO-Bi_2Te_3@PU) were applied to the wound and irradiated with NIR laser for three cycles. Afterward, the treated wounds were covered with nonwoven fabrics and fixed with surgical adhesive.

Bacteria in the wound were counted at specific time points using the spread plate method. At the same time, the wounds were regularly observed and photographed. After the rats were euthanized, the tissue around the wounds was removed for H&E, Masson's and Sirius Red staining. To evaluate in vivo biosafety, the major organs (heart, liver, spleen, lung, and kidney) were stained with H&E on day 12.

Statistical Analysis: All quantitative data were not pre-processed and expressed as mean values ± standard deviations (SD) (n = 3 independent samples). All statistical data were processed by GraphPad Prism or Origin software and statistical differences were analyzed by one-way analysis of variance (ANOVA) with Tukey's post hoc test, two-way ANOVA with Sidak's or Tukey's post hoc test, and a two-tailed Student's t-test (*$p < 0.05$, **$p < 0.01$, ***$p < 0.001$, ****$p < 0.0001$, and ns = no significant difference).

Supporting Information

Supporting Information is available from the Wiley Online Library or from the author.

Acknowledgements

This work was jointly supported by the National Natural Science Foundation of China (Nos. 51871162, 52173251, 82002303), the China National Funds for Distinguished Young Scholars (No. 51925104), the Central Guidance on Local Science and Technology Development Fund of Hebei Province (226Z1303G), Scientific Research Foundation of Peking University Shenzhen Hospital (KYQD2021064), Guangdong Basic and Applied Basic Research Foundation (2021A1515220093, 2022A1515011536) and NSFC-Guangdong Province Joint Program (Key program no. U21A2084).

Conflict of Interest

The authors declare no conflict of interest.

Data Availability Statement

The data that support the findings of this study are available in the supplementary material of this article.

Keywords

antibacterial, Bi_2Te_3, catalyses, photo-thermoelectric, wound healing

Received: August 31, 2022
Revised: October 19, 2022
Published online: November 7, 2022

[1] a) Z. Zhou, J. Li, L. Tan, X. Liu, Y. Zheng, Z. Cui, C. Li, K. W. K. Yeung, Z. Li, Y. Liang, S. Zhu, S. Wu, *Fundam. Res.* **2022**, *2*, 496; b) J. Li, Z. Zhou, X. Liu, Y. Zheng, C. Li, Z. Cui, K. W. K. Yeung, H. Zhou, J. Zou, Z. Li, S. Zhu, Y. Liang, X. Wang, S. Wu, *Matter* **2021**, *4*, 3030; c) Y. Qiao, Y. Xu, X. Liu, Y. Zheng, B. Li, Y. Han, Z. Li, K. W. K. Yeung, Y. Liang, S. Zhu, Z. Cui, S. Wu, *Nat. Commun.* **2022**, *13*, 2461; d) L. Jin, X. Liu, Y. Zheng, Z. Li, Y. Zhang, S. Zhu, H. Jiang, Z. Cui, P. K. Chu, S. Wu, *Adv. Funct. Mater.* **2022**, *32*, 2204437; e) H. Liu, J. Li, X. Liu, Z. Li, Y. Zhang, Y. Liang, Y. Zheng, S. Zhu, Z. Cui, S. Wu, *ACS Nano* **2021**, *15*, 18505.

[2] a) X. Kong, X. Liu, Y. Zheng, P. K. Chu, Y. Zhang, S. Wu, *Mater Sci Eng R Rep* **2021**, *145*, 100610; b) J. Li, X. Liu, L. Tan, Z. Cui, X. Yang, Y. Liang, Z. Li, S. Zhu, Y. Zheng, K. W. K. Yeung, X. Wang, S. Wu, *Nat. Commun.* **2019**, *10*, 4490.

[3] a) D. Huang, S. Chen, G. Zeng, X. Gong, C. Zhou, M. Cheng, W. Xue, X. Yan, J. Li, *Coord. Chem. Rev.* **2019**, *385*, 44; b) M. Yang, S. Qiu, E. Coy, S. Li, K. Zaleski, Y. Zhang, H. Pan, G. Wang, *Adv. Mater.* **2022**, *34*, 2106314.

[4] a) Z. Zhao, H. Zhou, L. Zheng, P. Niu, G. Yang, W. Hu, J. Ran, S. Qiao, J. Wang, H. Zheng, *Nano Energy* **2017**, *42*, 90; b) R. Tang, S. Zhou, Z. Yuan, L. Yin, *Adv. Funct. Mater.* **2017**, *27*, 1701102; c) J. Li, L. Cai, J. Shang, Y. Yu, L. Zhang, *Adv. Mater.* **2016**, *28*, 4059.

[5] a) D. Zhang, Y. Wang, Y. Yang, *Small* **2019**, *15*, 1805241; b) Y. Yang, K. C. Pradel, Q. Jing, J. M. Wu, F. Zhang, Y. Zhou, Y. Zhang, Z. L. Wang, *ACS Nano* **2012**, *6*, 6984.

[6] a) J. Li, Z. Li, X. Liu, C. Li, Y. Zheng, K. W. K. Yeung, Z. Cui, Y. Liang, S. Zhu, W. Hu, Y. Qi, T. Zhang, X. Wang, S. Wu, *Nat. Commun.* **2021**, *12*, 1224; b) Y. Li, X. Liu, L. Tan, Z. Cui, D. Jing, X. Yang, Y. Liang, Z. Li, S. Zhu, Y. Zheng, K. W. K. Yeung, D. Zheng, X. Wang, S. Wu, *Adv. Funct. Mater.* **2019**, *29*, 1900946.

[7] G. J. Snyder, E. S. Toberer, *Nat. Mater.* **2008**, *7*, 105.

[8] a) X. L. Shi, J. Zou, Z. G. Chen, *Chem. Rev.* **2020**, *120*, 7399; b) G. Tan, L. D. Zhao, M. G. Kanatzidis, *Chem. Rev.* **2016**, *116*, 12123.

[9] a) Y. Pei, X. Shi, A. LaLonde, H. Wang, L. Chen, G. J. Snyder, *Nature* **2011**, *473*, 66; b) Y. Huang, B. Zhang, J. Li, Z. Zhou, S. Zheng, N. Li, G. Wang, D. Zhang, D. Zhang, G. Han, G. Wang, X. Han, X. Lu, X. Zhou, *Adv. Mater.* **2022**, *34*, 2109952; c) Y. Xiao, H. Wu, W. Li, M. Yin, Y. Pei, Y. Zhang, L. Fu, Y. Chen, S. J. Pennycook, L. Huang, J. He, L. D. Zhao, *J. Am. Chem. Soc.* **2017**, *139*, 18732; d) S. Roychowdhury, T. Ghosh, R. Arora, U. V. Waghmare, K. Biswas, *Angew. Chem., Int. Ed.* **2018**, *57*, 15167.

[10] a) Z. Chen, X. Zhang, Y. Pei, *Adv. Mater.* **2018**, *30*, 1705617; b) C. Hu, K. Xia, C. Fu, X. Zhao, T. Zhu, *Energy Environ. Sci.* **2022**, *15*, 1406.

[11] R. Venkatasubramanian, E. Siivola, T. Colpitts, B. O'Quinn, *Nature* **2001**, *413*, 597.

[12] Y. Li, X. Bai, D. Yuan, F. Zhang, B. Li, X. San, B. Liang, S. Wang, J. Luo, G. Fu, *Nat. Commun.* **2022**, *13*, 776.

[13] Y. Jiang, X. Zhang, Y. Wang, N. Wang, D. West, S. Zhang, Z. Zhang, *Nano Lett.* **2015**, *15*, 3147.

[14] J. Yao, G. Yang, *Small* **2018**, *14*, 1704524.

[15] Q. Zhang, Y. Yan, G. Chen, *Adv. Sci.* **2015**, *2*, 1500176.

[16] a) N. Zhang, F. Zheng, B. Huang, Y. Ji, Q. Shao, Y. Li, X. Xiao, X. Huang, *Adv. Mater.* **2020**, *32*, 1906477; b) Y. Liu, Y. Zhang, K. H. Lim, M. Ibáñez, S. Ortega, M. Li, J. David, S. Martí-Sánchez, K. M. Ng, J. Arbiol, M. V. Kovalenko, D. Cadavid, A. Cabot, *ACS Nano* **2018**, *12*, 7174; c) S. Li, T. Fan, X. Liu, F. Liu, H. Meng, Y. Liu, F. Pan, *ACS Appl. Mater. Interfaces* **2017**, *9*, 3677.

[17] L. Tang, Y. Wang, Y. Li, H. Feng, J. Lu, J. Li, *Adv. Funct. Mater.* **2009**, *19*, 2782.

[18] A. C. Ferrari, D. M. Basko, *Nat. Nanotechnol.* **2013**, *8*, 235.

[19] H. Moussa, E. Girot, K. Mozet, H. Alem, G. Medjahdi, R. Schneider, *Appl. Catal. B* **2016**, *185*, 11.

[20] Y.-X. Duan, K.-H. Liu, Q. Zhang, J.-M. Yan, Q. Jiang, *Small Methods* **2020**, *4*, 1900846.

[21] N. Hussain, Q. Zhang, J. Lang, R. Zhang, M. Muhammad, K. Huang, T. Cosseron De Villenoisy, H. Ya, A. Karim, H. Wu, *Adv. Opt. Mater.* **2018**, *6*, 1701322.

[22] X. Zhang, X. Liu, C. Zhang, S. Peng, H. Zhou, L. He, J. Gou, X. Wang, J. Wang, *ACS Nano* **2022**, *16*, 4851.

[23] C. R. Thomas, M. K. Vallon, M. G. Frith, H. Sezen, S. K. Kushwaha, R. J. Cava, J. Schwartz, S. L. Bernasek, *Chem. Mater.* **2016**, *28*, 35.

[24] D. Zhao, Y. Wang, C.-L. Dong, Y.-C. Huang, J. Chen, F. Xue, S. Shen, L. Guo, *Nat. Energy* **2021**, *6*, 388.

[25] Z. Bu, X. Zhang, Y. Hu, Z. Chen, S. Lin, W. Li, C. Xiao, Y. Pei, *Nat. Commun.* **2022**, *13*, 237.

[26] Y. Yang, C. Zhang, D. Huang, G. Zeng, J. Huang, C. Lai, C. Zhou, W. Wang, H. Guo, W. Xue, R. Deng, M. Cheng, W. Xiong, *Appl. Catal. B* **2019**, *245*, 87.

[27] M. Sendner, P. K. Nayak, D. A. Egger, S. Beck, C. Müller, B. Epding, W. Kowalsky, L. Kronik, H. J. Snaith, A. Pucci, R. Lovrinčić, *Mater. Horiz.* **2016**, *3*, 613.

[28] M. Kim, S. I. Kim, S. W. Kim, H. S. Kim, K. H. Lee, *Adv. Mater.* **2021**, *33*, 2005931.

[29] J. J. Kuo, M. Wood, T. J. Slade, M. G. Kanatzidis, G. J. Snyder, *Energy Environ. Sci.* **2020**, *13*, 1250.

[30] C. Chang, M. Wu, D. He, Y. Pei, C.-F. Wu, X. Wu, H. Yu, F. Zhu, K. Wang, Y. Chen, L. Huang, J.-F. Li, J. He, L.-D. Zhao, *Science* **2018**, *360*, 778.

[31] K. Biswas, J. He, I. D. Blum, C. I. Wu, T. P. Hogan, D. N. Seidman, V. P. Dravid, M. G. Kanatzidis, *Nature* **2012**, *489*, 414.
[32] M. Li, D. L. Cortie, J. Liu, D. Yu, S. M. K. N. Islam, L. Zhao, D. R. G. Mitchell, R. A. Mole, M. B. Cortie, S. Dou, X. Wang, *Nano Energy* **2018**, *53*, 993.
[33] L. Gross, F. Mohn, P. Liljeroth, J. Repp, F. J. Giessibl, G. Meyer, *Science* **2009**, *324*, 1428.
[34] a) J.-Y. Ma, J. Ding, H.-J. Yan, D. Wang, J.-S. Hu, *ACS Appl. Mater. Interfaces* **2019**, *11*, 21627; b) S. Wang, Y. Gao, S. Miao, T. Liu, L. Mu, R. Li, F. Fan, C. Li, *J. Am. Chem. Soc.* **2017**, *139*, 11771.
[35] G. J. Snyder, A. H. Snyder, M. Wood, R. Gurunathan, B. H. Snyder, C. Niu, *Adv. Mater.* **2020**, *32*, 2001537.
[36] H.-S. Kim, Z. M. Gibbs, Y. Tang, H. Wang, G. J. Snyder, *APL Mater.* **2015**, *3*, 041506.

ADVANCED FUNCTIONAL MATERIALS

Supporting Information

for *Adv. Funct. Mater.,* DOI: 10.1002/adfm.202210098

Reduced Graphene Oxides Modified Bi_2Te_3 Nanosheets for Rapid Photo-Thermoelectric Catalytic Therapy of Bacteria-Infected Wounds

*Siyu Wang, Yuqian Qiao, Xiangmei Liu, Shengli Zhu, Yufeng Zheng, Hui Jiang, Yu Zhang, Jie Shen, Zhaoyang Li, Yanqin Liang, Zhenduo Cui, Paul K. Chu, and Shuilin Wu**

Supporting Information

Reduced Graphene Oxides Modified Bi_2Te_3 Nanosheets for Rapid Photo-Thermoelectric Catalytic Therapy of Bacteria-Infected Wounds

Siyu Wang, Yuqian Qiao, Xiangmei Liu, Shengli Zhu, Yufeng Zheng, Hui Jiang, Yu Zhang, Jie Shen, Zhaoyang Li, Yanqin Liang, Zhenduo Cui, Paul K Chu, Shuilin Wu*

S. Wang, Prof. S. Zhu, Prof. H. Jiang, Prof. Z. Li, Prof. Y. Liang, Prof. Z. Cui, Prof. S. Wu
School of Materials Science & Engineering, the Key Laboratory of Advanced Ceramics and Machining Technology by the Ministry of Education of China, Tianjin University, Tianjin 300072, China
E-mail: shuilinwu@tju.edu.cn

Dr. Y. Qiao, Prof. Y. Zheng, Prof. S. Wu
School of Materials Science & Engineering, Peking University, Beijing, 100871, China
E-mail: slwu@pku.edu.cn

Prof. X. Liu
School of Health Science and Biomedical Engineering, Hebei University of Technology, Xiping Avenue 5340, Beichen District, Tianjin 300401, China

Prof. Y. Zhang
Department of Orthopedics, Guangdong Provincial People's Hospital, Guangdong Academy of Medical Sciences, Guangzhou, 510080, China

Prof. J. Shen
Shenzhen Key Laboratory of Spine Surgery, Department of Spine Surgery, Peking University Shenzhen Hospital, Shenzhen, China

Prof. P.K. Chu
Department of Physics, Department of Materials Science and Engineering, and Department of Biomedical Engineering, City University of Hong Kong, Kowloon 999077, Hong Kong, China

Figures

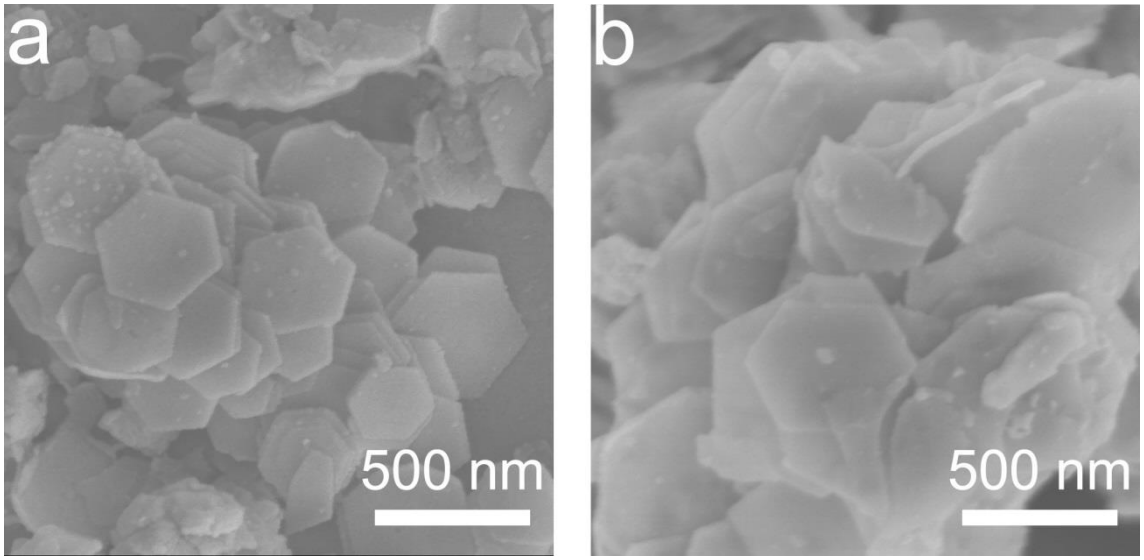

Figure S1. SEM image of a) Bi_2Te_3 and b) rGO-Bi_2Te_3.

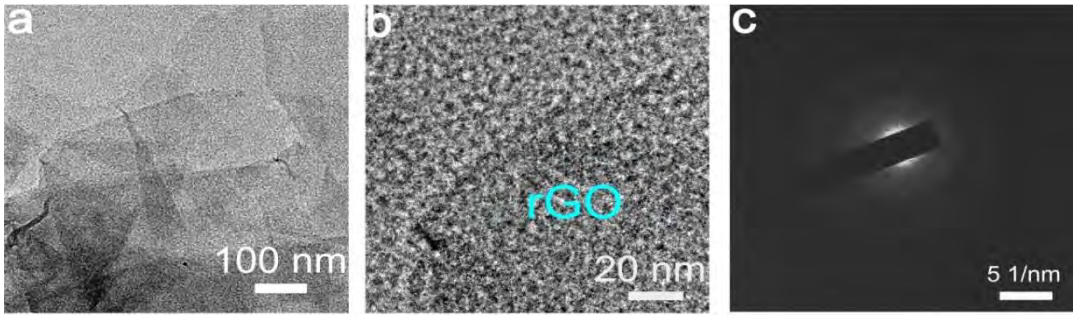

Figure S2. a) TEM image, b) HRTEM image, c) SAED pattern of rGO.

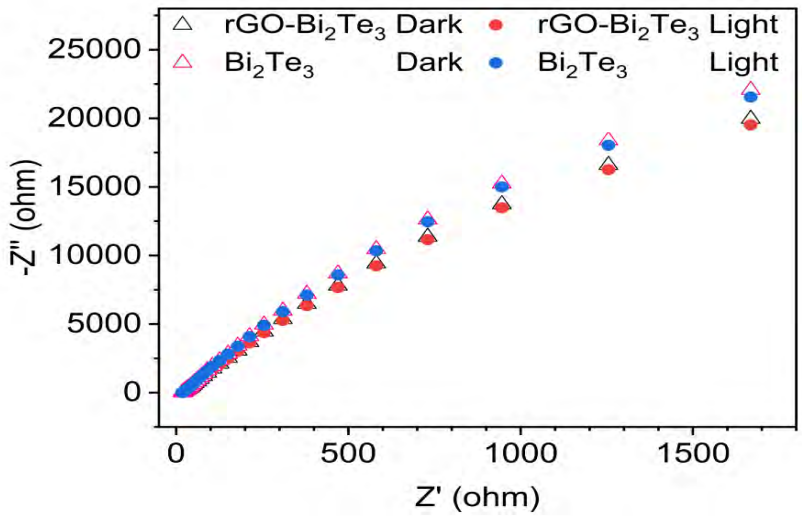

Figure S3. EIS spectra of Bi_2Te_3 and rGO-Bi_2Te_3 in 808 nm light and dark.

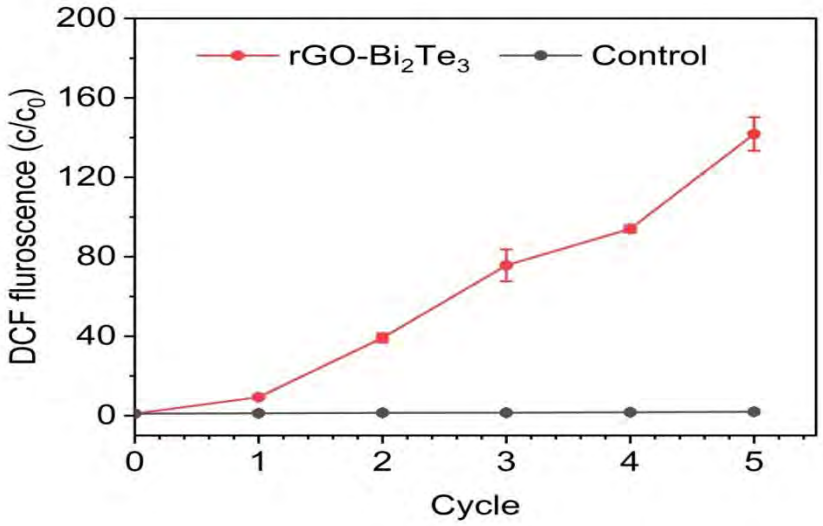

Figure S4. ROS production of rGO-Bi_2Te_3 by DCFH fluorescence probe under heating in 55 ^{o}C water bath without 808 nm NIR light. Individual data points (n = 3 independent samples) and error bar indicates mean ± SD.

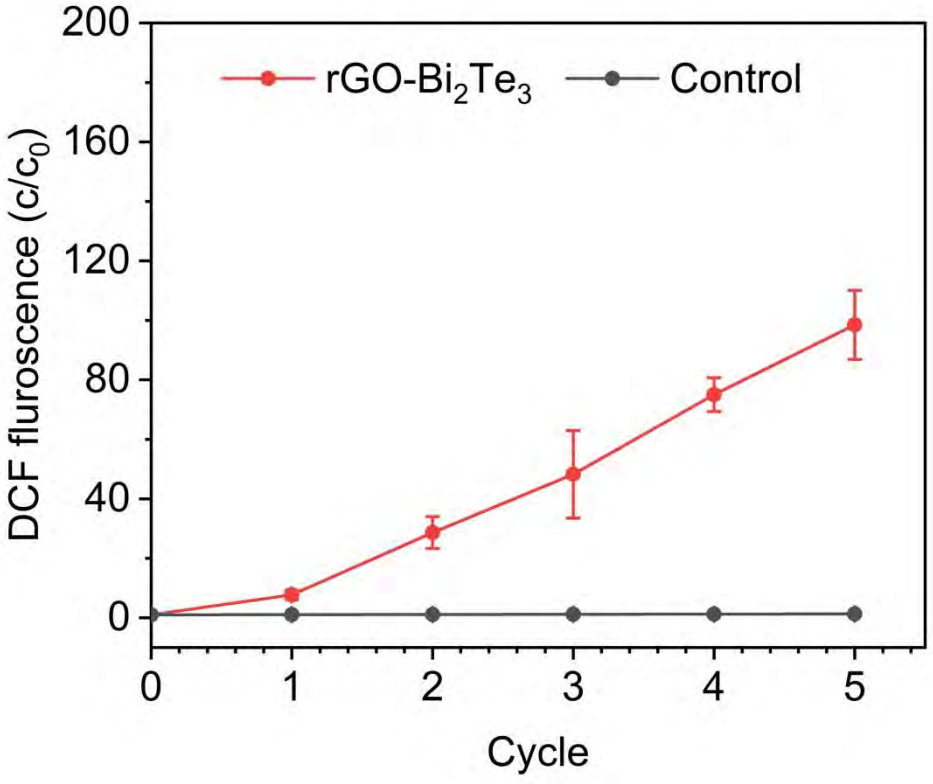

Figure S5. ROS production of rGO-Bi_2Te_3 by DCFH fluorescence probe under 808 nm NIR light irradiation (0.4 W cm^{-2}) in ice-water bath. Individual data points (n = 3 independent samples) and error bar indicates mean ± SD.

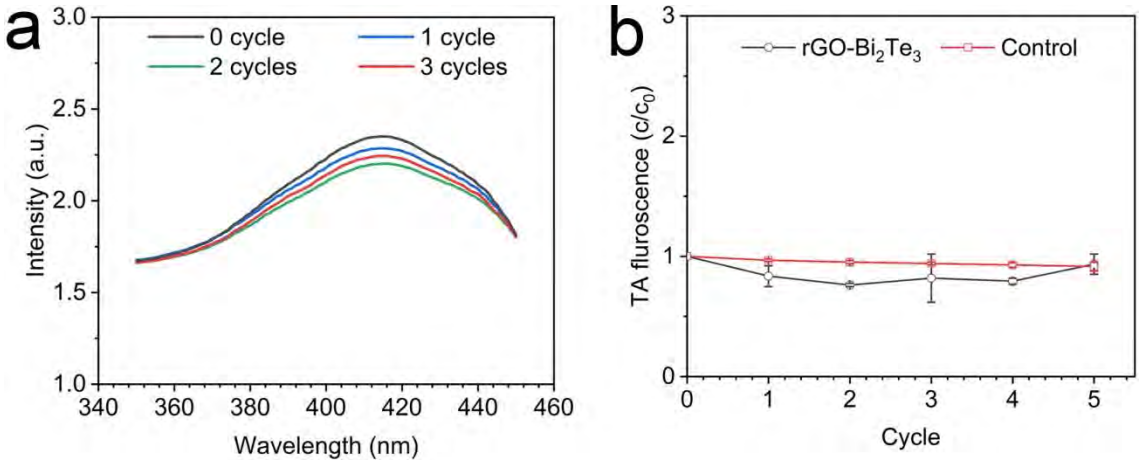

Figure S6. a) The detection of $^1O_2$ by DPBF, b) The detection of ·OH by under 808 nm light (0.4 W cm^{-2}) irradiation. Individual data points (n = 3 independent samples) and error bar indicates mean ± SD.

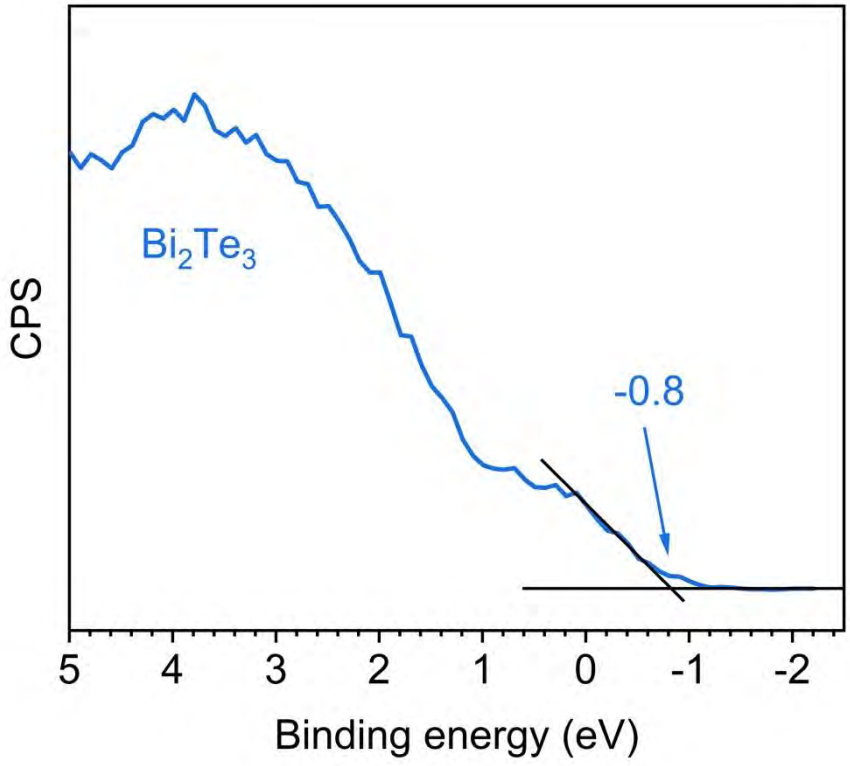

Figure S7. Valence band XPS spectrum of Bi_2Te_3 nanosheets.

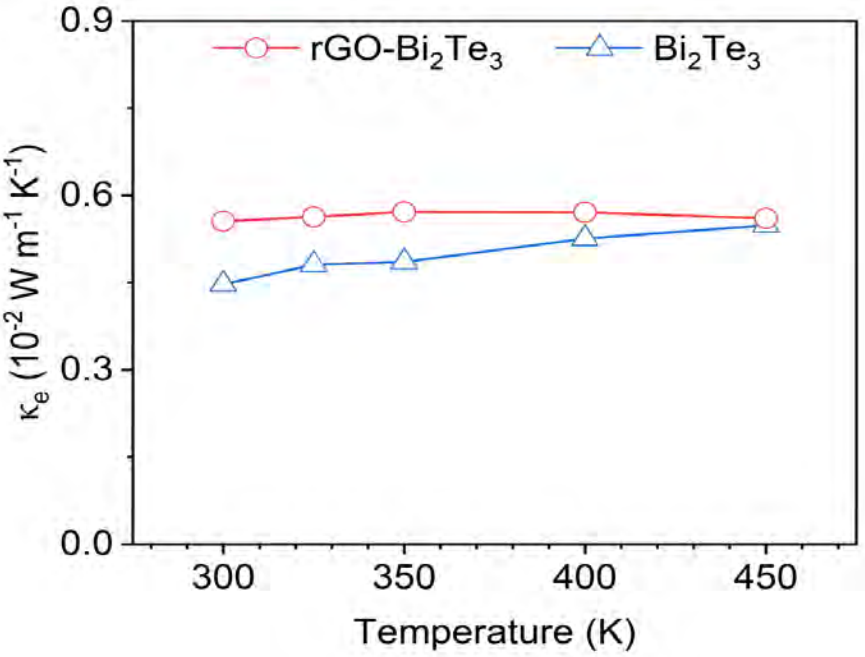

Figure S8. Thermoelectric properties of Bi_2Te_3 and rGO-Bi_2Te_3. Electric thermal conductivity.

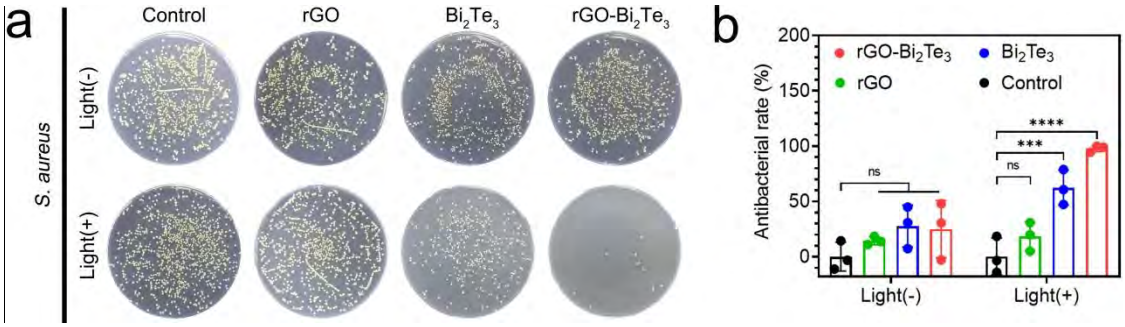

Figure S9. Antibacterial activity of the synthesized powder samples *in vitro*. a**)** Spread plate results and b) the histograms of the antibacterial efficiency of *S. aureus*. Individual data points (n = 3 biologically independent samples) and error bar indicates mean ± SD. Statistical differences were analyzed by two-way ANOVA with Tukey's post hoc test (***$P < 0.001$, ****$P < 0.0001$, *ns* = no significant difference).

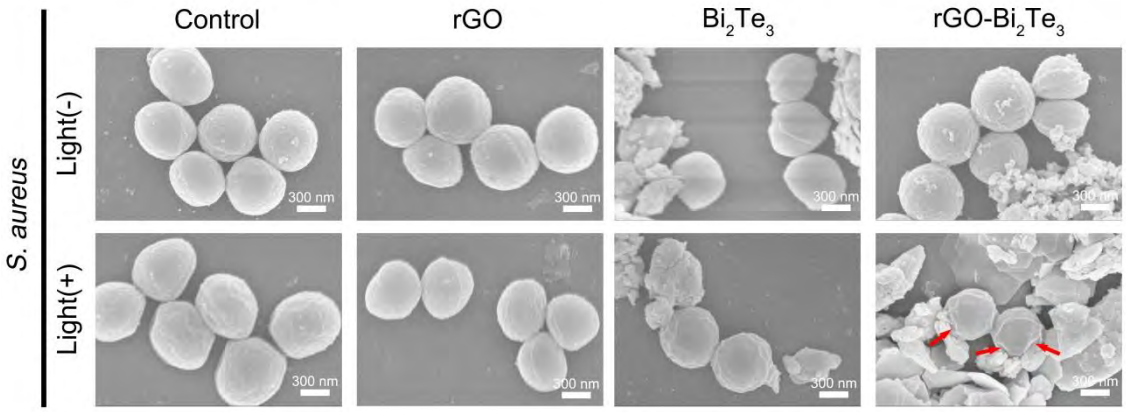

Figure S10. Antibacterial activity of the synthesized powder samples *in vitro*. SEM morphologies of *S. aureus* after irradiation or dark treatment.

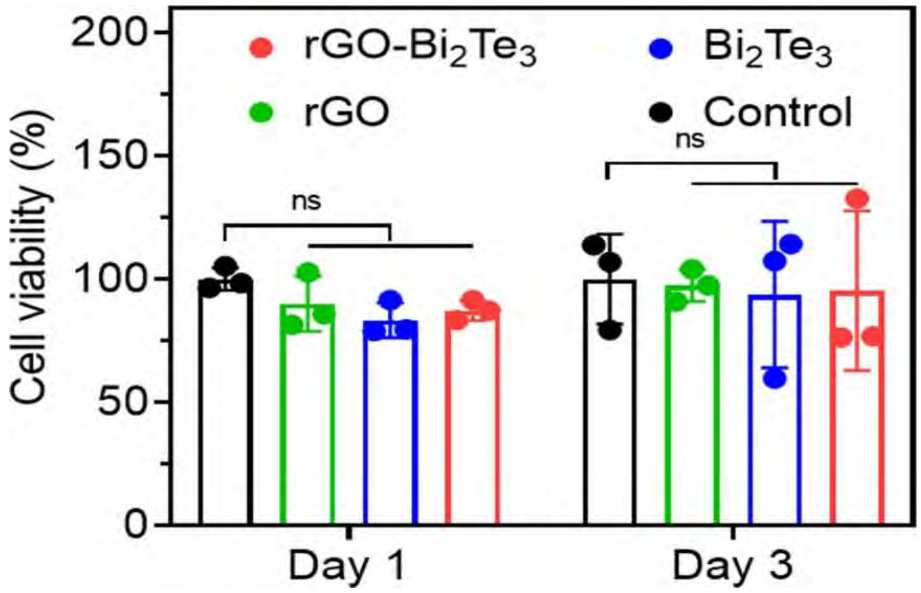

Figure S11. Cell viability of NIH-3T3 cells cultured with different samples and incubation for 1d and 3d at 37 ^{o}C. Individual data points (n = 3 biologically independent samples) and error bar indicates mean ± SD. Statistical differences were analyzed by one-way ANOVA with Tukey's post hoc test (*ns* = no significant difference).

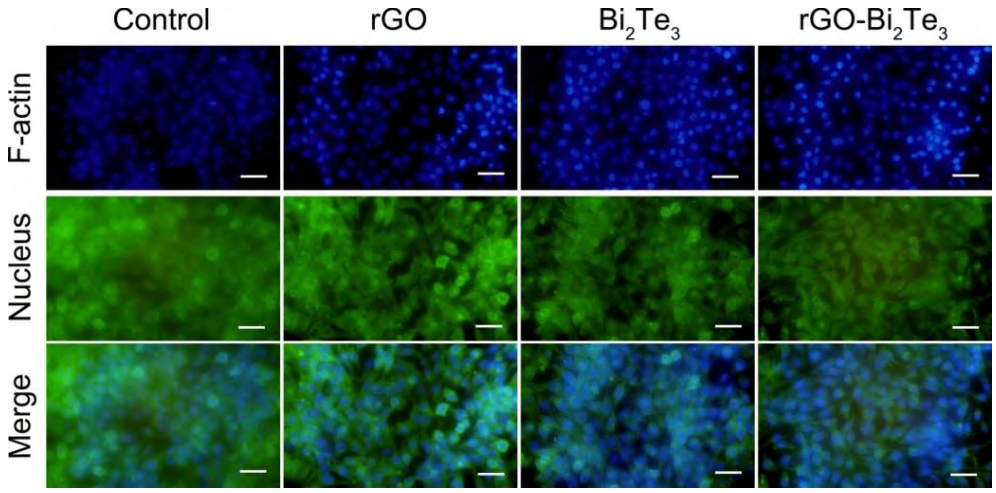

Figure S12. Fluorescent images of NIH-3T3 cells after co-cultured with different samples and incubation for 24 h at 37 °C; F-actin stained with FITC (green) and nucleus stained with DAPI (blue) (scale bars = 50 μm).

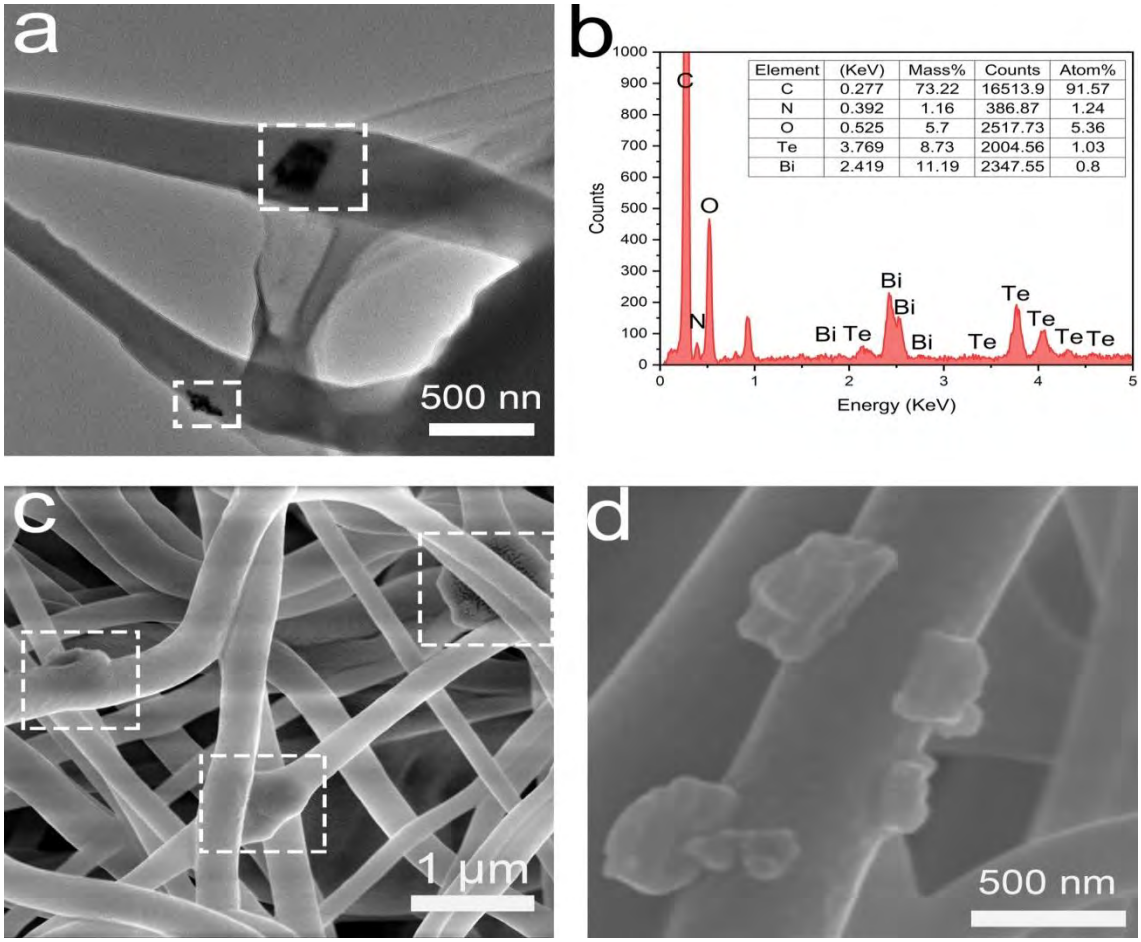

Figure S13. a) TEM image, b) EDS results, c) d) SEM image of 50% rGO-Bi_2Te_3@PU.

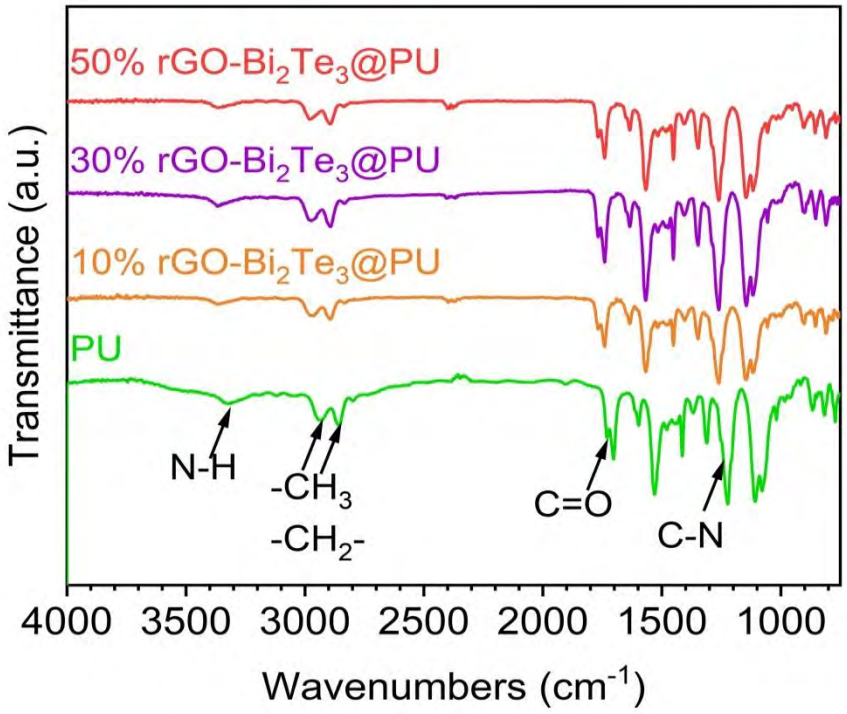

Figure S14. FTIR spectra of electrospinning membranes.

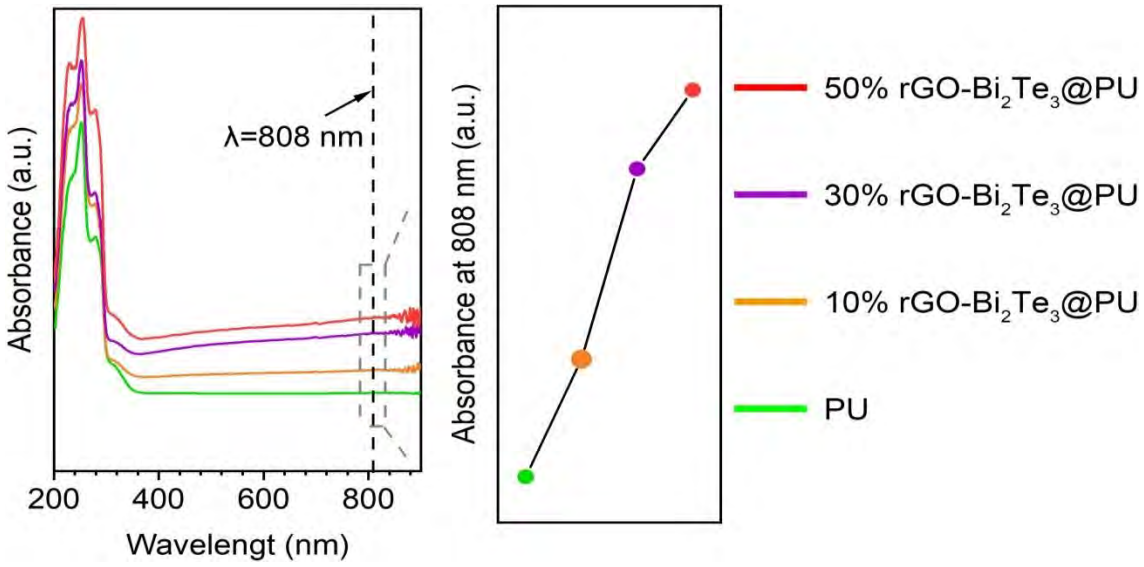

Figure S15. UV-vis-NIR spectrum of electrospinning membranes.

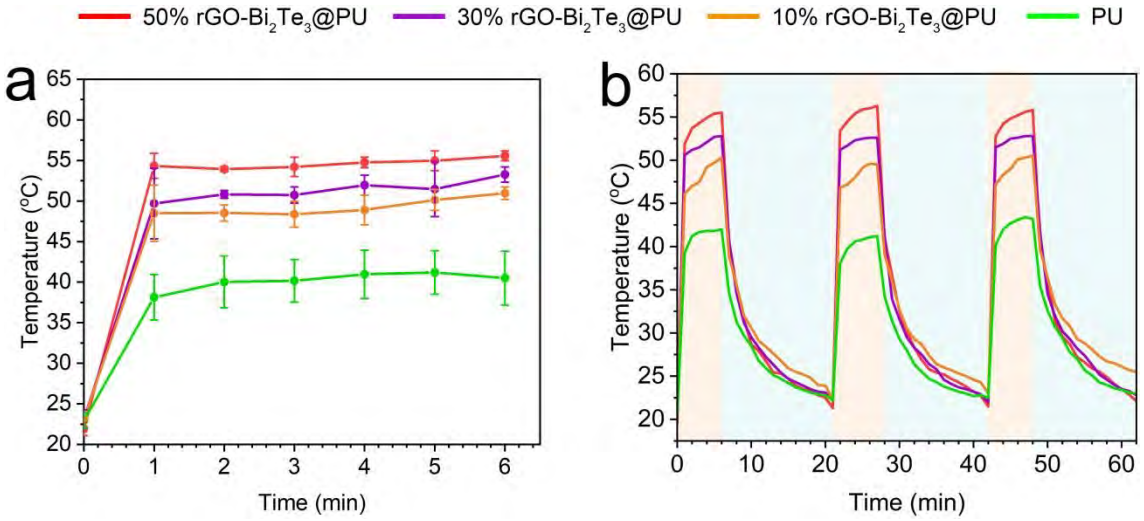

Figure S16. a**)** Photothermal curves and b**)** photothermal stability curves of electrospinning membranes. (808 nm NIR light, 0.2 W cm^{-2}, 6 min). Individual data points (n = 3 independent samples) and error bar indicates mean ± SD.

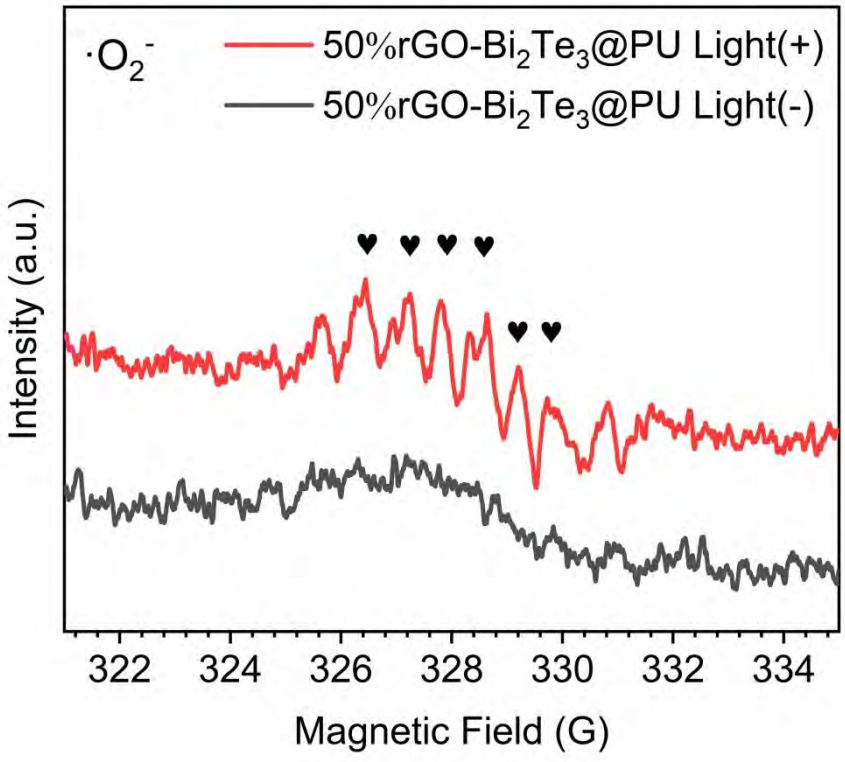

Figure S17. ESR spectra of 50% rGO-Bi_2Te_3@PU with and without 808 nm light irradiation.

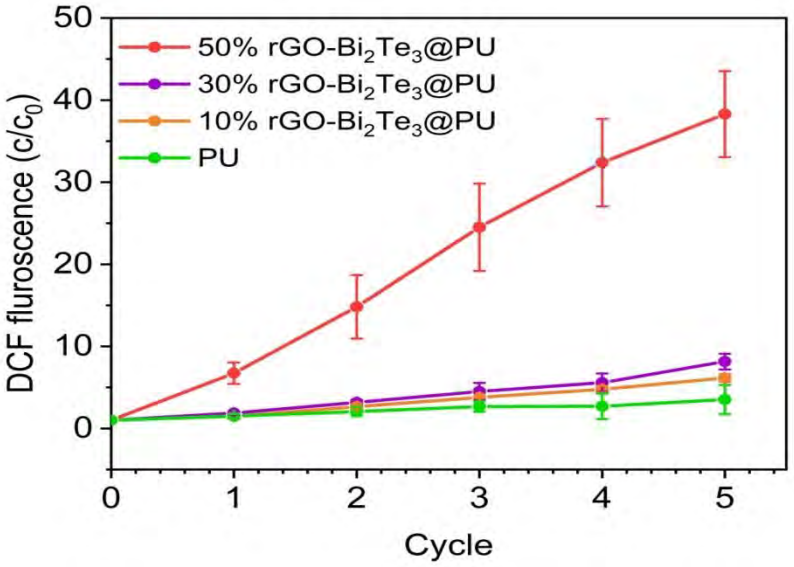

Figure S18. ROS production with DCFH fluorescence probe. Individual data points (n = 3 independent samples) and error bar indicates mean ± SD.

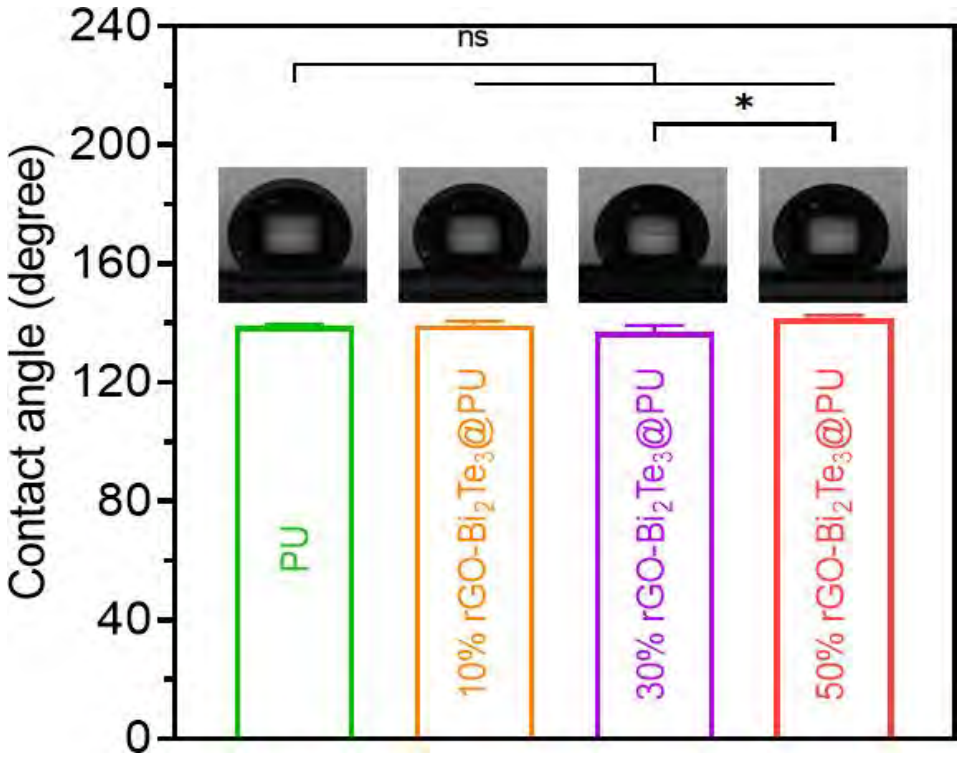

Figure S19. Water contact angle measurements of PU, 10% rGO-Bi_2Te_3@PU, 30% rGO-Bi_2Te_3@PU and 50% rGO-Bi_2Te_3@PU. Individual data points (n = 3 independent samples) and error bar indicates mean ± SD. Statistical differences were analyzed by one-way ANOVA with Tukey's post hoc test (*$P < 0.05$, *ns* = no significant difference).

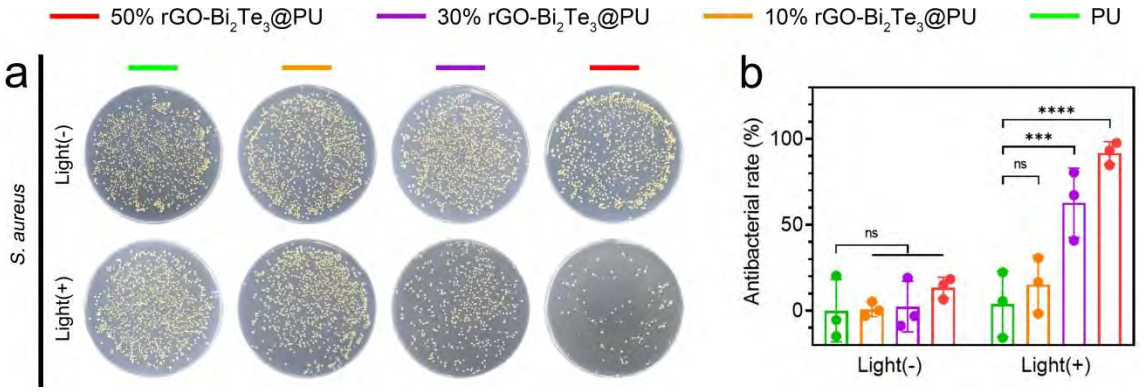

Figure S20. Antibacterial activity of spun membranes *in vitro*. a) Spread plate results and b) The histograms of the antibacterial efficiency of *S. aureus*. Individual data points (n = 3 biologically independent samples) and error bar indicates mean ± SD. Statistical differences were analyzed by two-way ANOVA with Sidak's post hoc test (***P < 0.001, ****P < 0.0001, *ns* = no significant difference).

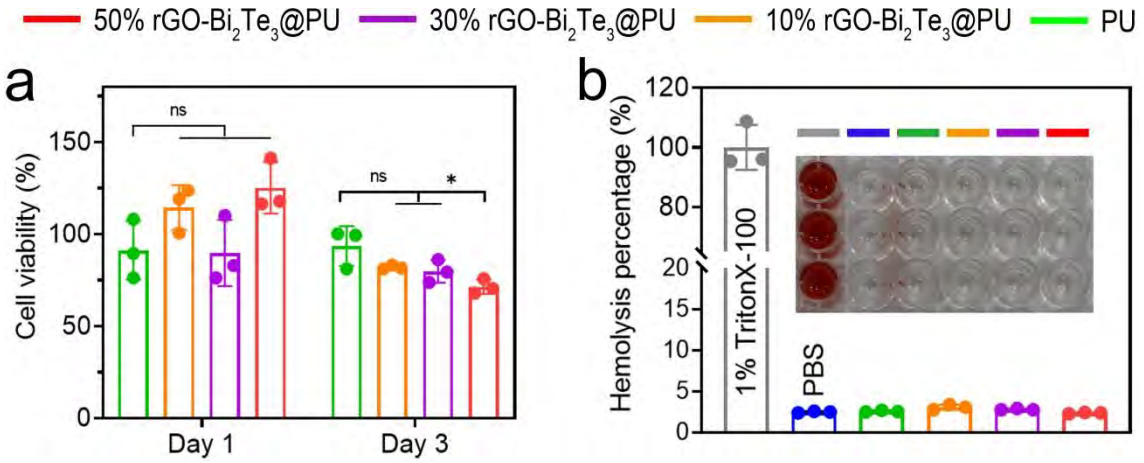

Figure S21. a) Cell viability of NIH-3T3 cells cultured with different spun membranes and incubation for 1d and 3d at 37 °C. b) Evaluation hemolysis of different spun membranes. 1% TritonX-100 and PBS were used as positive control group and negative control group, respectively. Individual data points (n = 3 biologically independent samples) and error bar indicates mean ± SD. Statistical differences were analyzed by one-way ANOVA with Tukey's post hoc test (*P < 0.05, *ns* = no significant difference).

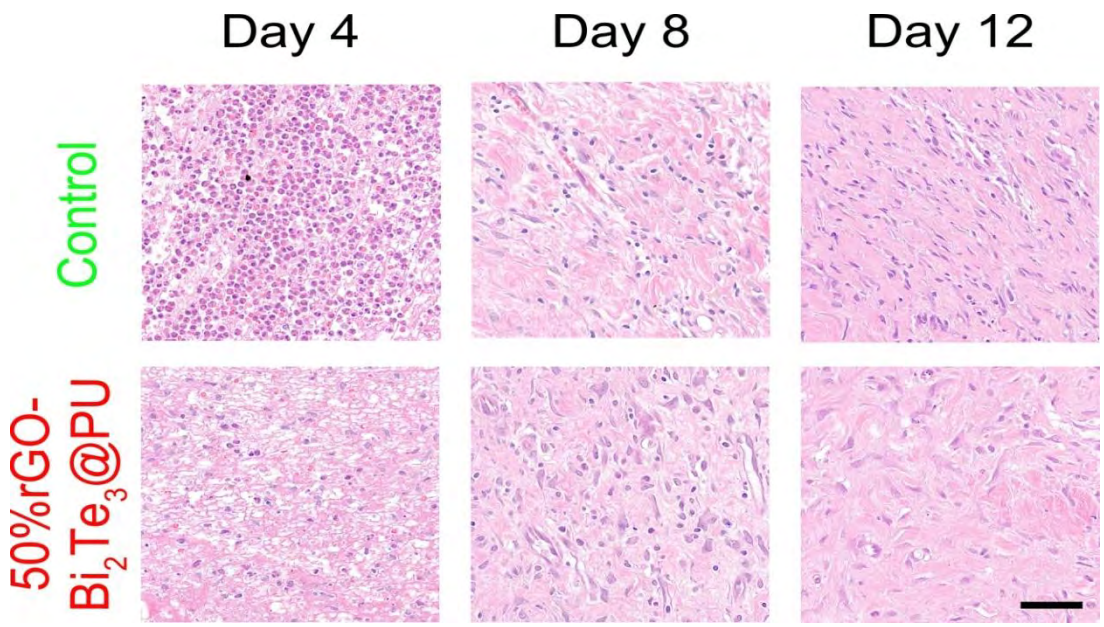

Figure S22. H&E staining of control and 50% rGO-Bi_2Te_3@PU groups at 4, 8, and 12 days (scale bars = 50 μm).

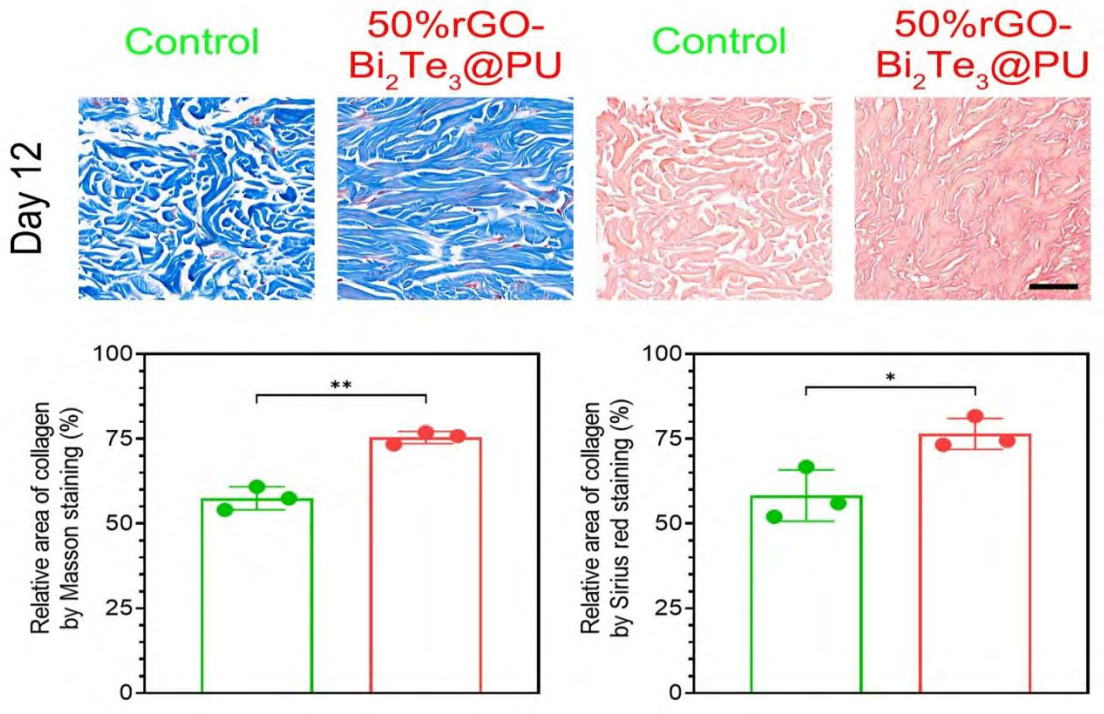

Figure S23. a) Masson's trichrome staining and Sirius red staining of control and 50% rGO-Bi_2Te_3@PU groups at 12 days (scale bars = 50 μm). Quantitatively relative area of collagen in corresponding. b) Masson's trichrome staining and c) Sirius red staining. Individual data points (n = 3 biologically independent samples) and error bar indicates mean ± SD. Statistical differences were analyzed by a two-tailed Student's t-test (*P < 0.05, **P < 0.01).

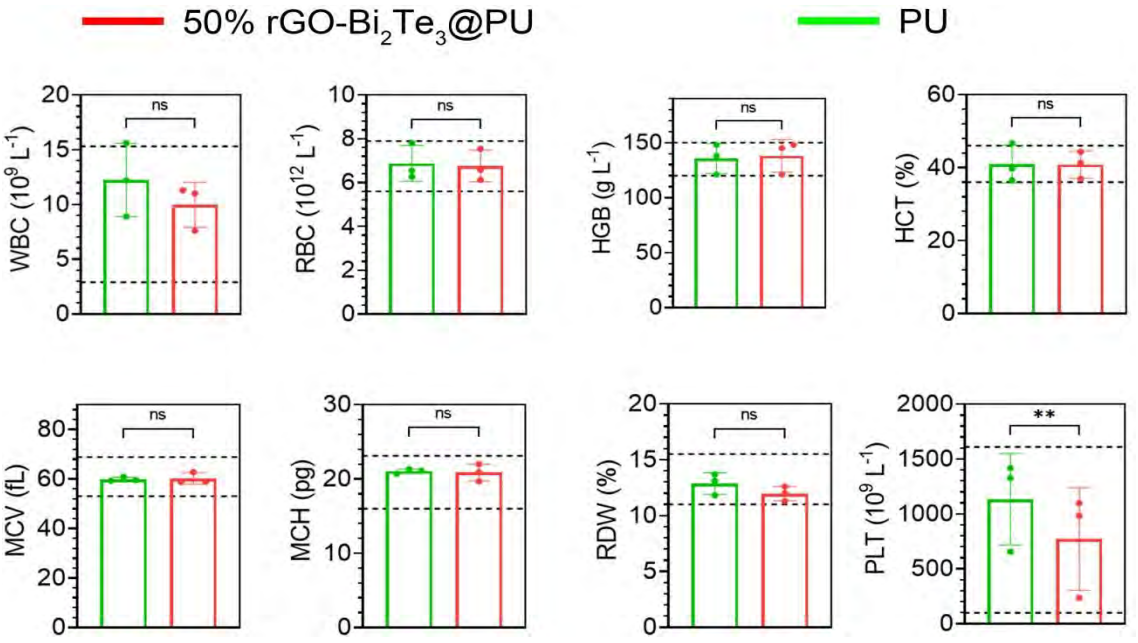

Figure S24. Data of standard hematology of control and 50% rGO-Bi_2Te_3@PU groups on day 12, including WBC, RBC, HGB, HCT, MCV, MCH, RDW, and PLT. Lines of dashes mark corresponding normal scope. Individual data points (n = 3 biologically independent samples) and error bar indicates mean ± SD. Statistical differences were analyzed by a two-tailed Student's t-test (**$P < 0.01$, *ns* = no significant difference).

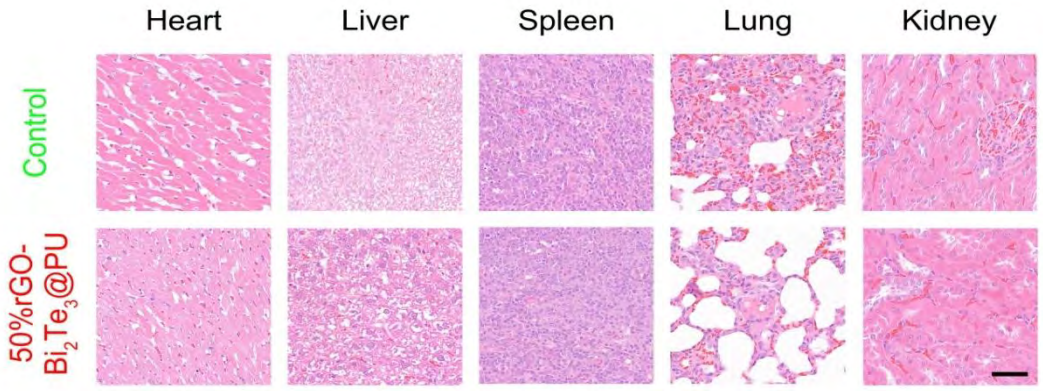

Figure S25. Histological analyses of major organs (liver, spleen, kidney, heart, and lung) on day 12 through H&E staining (scale bar = 100 μm).

Table S1. The measured heat capacity of Bi_2Te_3 and rGO-Bi_2Te_3 by Differential Scanning Calorimetry.

Sample	Temperature [K]	Heat flux [mW]	Quality [mg]	Specific heat capacity [J/g/K]
Bi_2Te_3	300	-0.815	24.55	0.209114167
Bi_2Te_3	325	-0.893	24.55	0.227138205
Bi_2Te_3	350	-0.99	24.55	0.237467017
Bi_2Te_3	400	-1.113	24.55	0.278677304
Bi_2Te_3	450	-1.155	24.55	0.287021083
rGO-Bi_2Te_3	300	-0.919	29.62	0.193260011
rGO-Bi_2Te_3	325	-0.996	29.62	0.20800553
rGO-Bi_2Te_3	350	-1.117	29.62	0.23120246
rGO-Bi_2Te_3	400	-1.248	29.62	0.256918266
rGO-Bi_2Te_3	450	-1.326	29.62	0.27059284